ASME Journal of Vibration and Acoustics
Online journal at:
https://asmedigitalcollection.asme.org/vibrationacoustics

Zhenkun Guo
School of Mechanical Engineering,
University of Science and Technology Beijing,
Beijing 100083, China;
School of Mechanical-Electronic and Vehicle Engineering,
Beijing University of Civil Engineering and Architecture,
Beijing 100044, China
e-mail: guozhenkun@bucea.edu.cn

Shuai Jiang
School of Mechanical Engineering,
University of Science and Technology Beijing,
Beijing 100083, China;
Internet of Things Thrust,
The Hong Kong University of Science and Technology (Guangzhou),
Guangzhou 511400, China;
School of Mechanical-Electronic and Vehicle Engineering,
Beijing University of Civil Engineering and Architecture,
Beijing 100044, China
e-mail: js1736957811@126.com

Chengyun Du
Internet of Things Thrust,
The Hong Kong University of Science and Technology (Guangzhou),
Guangzhou 511400, China
e-mail: chengyun_du@163.com

Ye Zhang
Internet of Things Thrust,
The Hong Kong University of Science and Technology (Guangzhou),
Guangzhou 511400, China
e-mail: m19544542711@163.com

Hao Tang
Internet of Things Thrust,
The Hong Kong University of Science and Technology (Guangzhou),
Guangzhou 511400, China
e-mail: htang969@connect.hkust-gz.edu.cn

Guobiao Hu[1]
Internet of Things Thrust,
The Hong Kong University of Science and Technology (Guangzhou),
Guangzhou 511400, China
e-mail: guobiaohu@hkust-gz.edu.cn

Enhanced Energy Harvesting With a Piezoelectric Diatomic Sandwich Beam Shunted to an SECE Circuit

This study introduces a novel piezoelectric energy harvester based on a diatomic sandwich beam structure, offering a promising solution for wireless sensors and IoT nodes to operate without chemical batteries. The dynamic model is derived using the homogenization theory and Hamilton's principle, with the electromechanical coupling model established via the Lagrange equation and modal assumptions. The model is verified through finite element analysis (FEM). The proposed sandwich beam outperforms a traditional uniform beam, yielding a 2.67-fold increase in voltage output, a 7.14-fold increase in power output, and a broader operational bandwidth. The effects of geometric and material parameters on energy efficiency are analyzed to guide design optimization. Additionally, a novel equivalent circuit model (ECM) for the piezoelectric diatomic sandwich beam (PDSB) is presented and integrated with a synchronized charge extraction (SECE) circuit, showing superior power stability and efficiency compared to a resistive shunt (RS) circuit. Finally, the PDSB shunted to the SECE circuit implemented on the printed circuit board is experimentally tested. This study provides valuable insights for the design and analysis of sandwich beam-based piezoelectric energy harvesters, thereby advancing their potential for practical applications. [DOI: 10.1115/1.4070071]

Keywords: vibration energy harvesting, interface circuits, piezoelectric diatomic sandwich beam, equivalent circuit model, synchronous electric charge extraction, dynamics, mechatronics and electromechanical systems, smart materials and structures

1 Introduction

In response to the worsening energy crisis and environmental problems, developing green and sustainable energy technologies

[1]Corresponding author.
Contributed by the Technical Committee on Vibration and Sound of ASME for publication in the Journal of Vibration and Acoustics. Manuscript received June 29, 2025; final manuscript received September 27, 2025; published online November 19, 2025. Assoc. Editor: Marcias Martinez.

has gained significant attention as a global research priority [1]. Of the various energy harvesting technologies [2–4], those leveraging mechanical vibrations have drawn considerable interest from academic and engineering communities due to their wide accessibility. Vibration energy harvesters can convert vibrations or other forms of kinetic energy into electricity [5–8], supplying power to low-power electronics such as sensors and medical implants. Despite significant advancements in the past two decades, current energy harvesting technologies still face huge challenges in efficiency, scalability, reliability, and durability. In particular, further breakthroughs are urgently needed to meet design requirements that balance lightweight and efficient energy conversion.

Sandwich structures are extensively employed in aerospace, civil engineering, automobile manufacturing, marine engineering, and numerous other fields due to their excellent mechanical properties [9–12]. From the perspective of static mechanics, previous studies have demonstrated their high load-bearing capacities, strong resistance to local buckling, and failure mechanisms of sandwich structures [13,14]. By employing theoretical analysis, finite element methods (FEM), and experimental testing, researchers have investigated how different materials and geometric parameters impact the static mechanics of sandwich structures. In recent years, in addition to static studies, researchers have also conducted extensive research on the dynamic characteristics of sandwich structures [15,16]. Li and Lv [17] applied the assumed modal method to study the active vibration control of pyramid sandwich beams with piezoelectric actuators/sensors. Zhao et al. [18] employed the assumed modal method combined with interpolation polynomials to analyze the free vibration of multi-span pyramid sandwich beams. Additionally, Li et al. [19] utilized the assumed modal method and performed vibration test experiments to explore the dynamic characteristics of multi-layer pyramid lattice sandwich beams.

Apart from traditional sandwich beams, metamaterial sandwich beams have also attracted widespread attention due to their unique mechanical properties. Zhang et al. [20] developed a pyramid sandwich metamaterial beam consisting of a hollow rod embedded with spring-mass resonators. Li et al. [21] presented the design of a single-phase super-pyramid sandwich panel based on metamaterial concepts, featuring broadband vibration suppression characteristics and improved load-bearing capacity. Guo et al. [22] designed an hourglass-shaped lattice sandwich structure for electric aircraft and evaluated the broadband low-frequency vibration reduction performance. Yu et al. [23] proposed an hourglass-shaped diatomic sandwich structure and conducted in-depth research on its topological performance. Guo et al. [24] researched the band gap characteristics of the hourglass-shaped diatomic sandwich beam structure using simulation and experiments. The above-mentioned studies primarily focused on the design methodologies and band gap generation mechanisms of metamaterial sandwich structures for low-frequency and broadband vibration suppression [25,26].

Although sandwich beams exhibit exceptional mechanical properties, their potential for energy harvesting remains largely underexplored. To fill this research gap, this paper provides a pioneering and comprehensive study, showcasing the promising potential and advantages of sandwich beams in enhancing energy harvesting performance. In recent years, the research on piezoelectric energy harvesters has attracted widespread attention [27,28] as vibration-based energy harvesters offer a promising alternative to external power sources and provide viable solutions to energy scarcity and pollution challenges [29–31]. Various methods for vibration energy harvesting and a lot of enhanced approaches have been developed [32,33]. Erturk and Inman [34] derived an analytical solution for cantilever beam-based piezoelectric harvesters and conducted a study on the case involving an unimorph piezoelectric patch. Subsequently, a correction factor was introduced to refine the commonly used single-degree-of-freedom (SDOF) model, thereby improving the accuracy of the SDOF model for both lateral and longitudinal vibrations [35]. Xiong and Oyadiji [36] performed an optimization for the cantilever piezoelectric vibration energy harvester through geometric modifications, employing a distributed parameter model and FEM. This optimization approach contributed to enhancing the efficiency of the piezoelectric energy harvester.

The studies mentioned above are all based on cantilever plain beam structures. Zhang et al. [37] introduced a multifunctional lattice sandwich structure that integrates energy harvesting and nonlinear vibration control, thereby expanding the application range of metamaterial-based energy harvesters. Li et al. [38] proposed a flexible piezoelectric energy harvester with a soft substrate sandwich beam and highlighted the significance of design factors such as substrate length and Young's modulus. Aewzipo et al. [39] designed a sandwich structure featuring a negative stiffness metamaterial core with unique mechanical properties such as shape recovery and energy absorption. These preliminary studies have demonstrated that composite beams can benefit piezoelectric energy harvesting performance and outperform traditional plain beams. Compared with multi-layered composite beams, sandwich beams have greater potential for piezoelectric energy harvesting applications due to their exceptional mechanical properties, optimized strain distribution, and high design flexibility. Sandwich structures can not only improve energy harvesting efficiency but also ensure system stability and durability, providing a viable solution for efficient and reliable energy harvesting. However, the research on this topic is still in its infancy.

In addition, circuit design plays a crucial role in affecting energy harvesting efficiency, and the integration of a piezoelectric energy harvester with various interface circuits has been extensively explored [40]. Lefeuvre et al. [41] first proposed the synchronous electric charge extraction (SECE) circuit to improve electromechanical conversion efficiency and address the impedance matching issue. Yang and Tang [42] established an equivalent circuit model (ECM) to integrate structural modeling with circuit simulation. Fang et al. [43] designed a broadband harvester for low-frequency rotation and presented the electromechanical model of the harvester and its response analysis under different connections and interface circuits. Zhang et al. [44] analyzed the energy harvesting performance of a piezoelectric energy harvester shunted to four different interface circuits. Clementi et al. [45] designed an equivalent circuit model of a dual-chip cantilever beam based on LiNbO3 and stainless steel and characterized its vibration energy harvesting performance. However, the mechanical structures used in the aforementioned studies are restricted to simple cantilever beam-based piezoelectric energy harvesters, while the integration of interface circuits with sandwich beam structures remains entirely unexplored. Therefore, to fill this research gap, this study, for the first time, explores the integration of a complex diatomic sandwich structure-based energy harvester with an SECE circuit, aiming to achieve a dual enhancement in energy harvesting efficiency from both mechanical and electrical design perspectives. The SECE interface circuit extracts the electrical energy stored in the piezoelectric element exactly at the voltage peak, rapidly transferring it to a storage element via an inductor. This controlled charge extraction mitigates the impedance mismatch problem and renders the harvested power largely independent of load resistance. Compared with traditional resistive shunt (RS) circuits, the SECE circuit achieves higher energy conversion efficiency, greater voltage stability under varying load conditions, and a broader operating bandwidth. By establishing an ECM for the proposed piezoelectric diatomic sandwich beam (PDSB) and integrating it with a self-powered SECE circuit, this study establishes a unified framework that enables systematic co-optimization of structural dynamics and interface electronics, paving the way for robust and high-efficiency energy harvesting in real-world variable-load environments.

The rest of this paper is organized as follows: Sec. 2 establishes the mathematical model of the proposed PDSB. In Sec. 3, the FEM results are compared with those of the theoretical model to verify the accuracy and reliability. In addition, the impacts of geometric and material parameters, including Young's modulus, strut

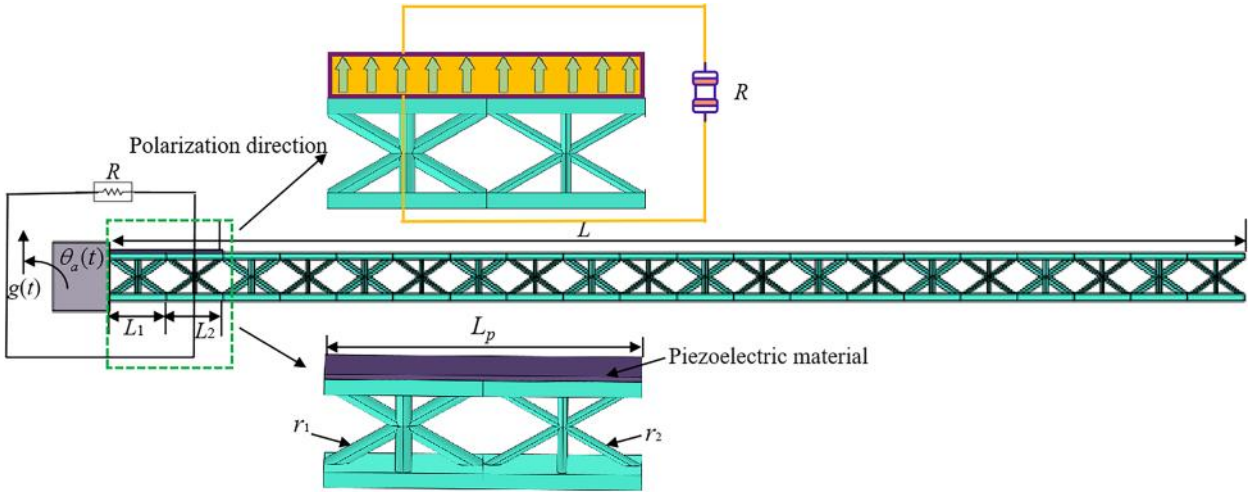

Fig. 1 Periodic PDSB structure with piezoelectric patch

radius, and core layer thickness, on the energy harvesting performance are analyzed. Section 4 examines the circuit interface characteristics and constructs the ECM of the PDSB structure for the first time, demonstrating the performance enhancement achieved with the SECE circuit. Section 5 presents an experimental validation. Finally, conclusions are summarized in Sec. 6.

2 Theoretical Formulation

This section presents the theoretical model of the PDSB. By applying the homogenization method, expressions for the kinetic, potential, and piezoelectric energies stored in the structure are derived. The electromechanically coupled dynamic equations of the PDSB are formulated using the Lagrange equation method and the assumed modal expansion theory.

2.1 Description of the Model. The proposed PDSB is shown in Fig. 1. The sandwich metastructure features a periodic unit design, where each unit consists of a sandwich base beam and two hourglass-shaped core elements. The hourglass element is composed of eight diagonal support struts with a radius of r_1 or r_2. In this paper, "diatomic" refers to the periodic alternation of structural parameters. Specifically, the strut radii, r_1 and r_2, alternate within the hourglass-shaped core to deliberately introduce impedance mismatch, thereby enabling vibration control. Although this arrangement can yield Bragg-type band gap properties similar to those found in phononic crystal structures [23–26], the present work focuses on investigating the vibration energy harvesting performance, rather than on wide bandgap engineering. Notably, the PDSB structure possesses a continuous geometry and single-phase material composition, thereby avoiding any special manufacturing requirements. The length and width of the substrate beams are denoted by L and b, respectively, and the length of the piezoelectric patch is L_p.

In developing the electromechanical model of the PDSB, the assumption of linear small deformations is adopted to characterize the elastic behavior. The following considerations are based on the distinctive properties of the substrate:

(a) Given the thinness of the top and bottom layers and the piezoelectric layer bonded on top, the normal stress in the thickness direction is deemed negligible.
(b) The velocity remains constant throughout the thickness of the surface layers, enabling the motion of the core layer to represent the beam's overall dynamic behavior.
(c) The deformations of the top and bottom beams, as well as the core layer, are decoupled in the thickness direction, considering the significant disparity in their Young's moduli. The line perpendicular to the neutral axis is divided into three distinct segments upon deformation. The shear deformations of the top and bottom beams and the piezoelectric layer are negligible. The core layer's shear deformation is assumed to be linear, given that the core is much thicker and more flexible than other layers.
(d) The layers are assumed to be ideally bonded, with the adhesive mass neglected.

Figure 2 illustrates the hourglass-shaped lattice unit of the sandwich beam, where β and l denote the inclination angle and length of the struts, respectively. The thicknesses of the top, bottom, core, and piezoelectric layers are represented by h_t, h_b, h_c, and h_d, respectively. The lattice constant can be calculated as $L_c = 4l\cos\beta$. The entire sandwich beam structure is made of the same material with a density of ρ_f, and the hourglass lattice truss core is modeled as a homogeneous soft material with equivalent densities $\overline{\rho_j} = \dfrac{\rho_j}{\rho_f} = \dfrac{2\pi r_j^2}{bl\cos\beta\sin\beta}(j = 1, 2)$. Similarly, the equivalent shear modulus is expressed as $G_j = \dfrac{\overline{\rho_j}}{8}E\sin^2 2\beta$, where E is Young's modulus. Under base excitation, the PDSB undergoes vibration, and the dynamic strain induced in the piezoelectric material generates an electrical charge, which is subsequently dissipated across a resistor. The base excitation applied to the PDSB is described as

$$w_c(x, t) = g(t) + x\theta_a(t), \tag{1}$$

where $g(t)$ and $\theta_a(t)$ represent the transverse displacement and rotation of the base, respectively.

Thus, the absolute displacement of the PDSB along the vertical axis is expressed by

$$w_a(x, t) = w(x, t) + w_c(x, t), \tag{2}$$

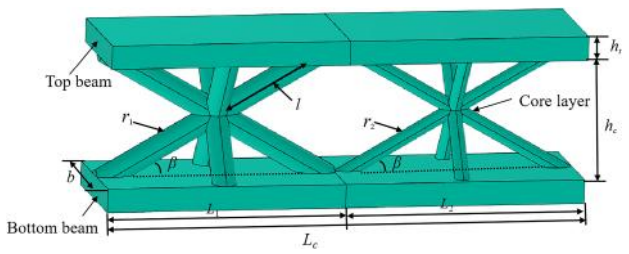

Fig. 2 Hourglass-shaped lattice unit of the sandwich beam

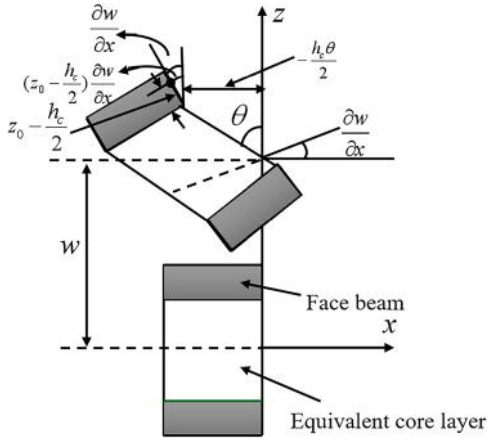

Fig. 3 Deformation diagram of a differential element in the sandwich beam

where $w(x,t)$ represents the transverse displacement of the core layer at position x and time t, relative to the moving base.

2.2 Energies in the PDSB. Figure 3 presents a schematic of the structural bending deformation of a differential element derived from the assumptions outlined previously. From the geometric relationships depicted in Fig. 3, the displacement at any point of the PDSB is expressed as follows [46]:

$$u_t = -\frac{h_c}{2}\theta - (z_0 - \frac{h_c}{2})\frac{\partial w_t}{\partial x}, \quad w_t = w, \tag{3a}$$

$$u_c^i = -z_0\theta, \quad w_c^i = w, \tag{3b}$$

$$u_b = \frac{h_c}{2}\theta - (z_0 + \frac{h_c}{2})\frac{\partial w_b}{\partial x}, \quad w_b = w, \tag{3c}$$

$$u_p = -\frac{h_c}{2}\theta - (z_0 - \frac{h_c}{2})\frac{\partial w_p}{\partial x}, \quad w_p = w, \tag{3d}$$

where z denotes the transverse coordinate axis of the PDSB, θ represents the rotation angle of the core layer under shear deformation, and $\partial w/\partial x$ corresponds to the rotation angle of the top and bottom beams under bending deformation. The displacement of the PDSB in the z-axis direction is denoted by w, while the axial displacements of the top beam, core layer, bottom beam, and piezoelectric layer are denoted by u_t, u_c^i $(i = 1, 2)$, u_b, and u_p. Similarly, the transverse displacements of the top, core, bottom, and piezoelectric layers are denoted by w_t, w_c^i, w_b, and w_p, respectively.

The strain–displacement relationship of the PDSB structure is expressed as follows:

$$\varepsilon_{tx} = -\frac{h_c}{2}\frac{\partial\theta}{\partial x} - (z_0 - \frac{h_c}{2})\frac{\partial^2 w}{\partial x^2}, \tag{4a}$$

$$\gamma_{cxz}^i = -\theta + \frac{\partial w}{\partial x}, \tag{4b}$$

$$\varepsilon_{bx} = \frac{h_c}{2}\frac{\partial\theta}{\partial x} - (z_0 + \frac{h_c}{2})\frac{\partial^2 w}{\partial x^2}, \tag{4c}$$

$$\varepsilon_{px} = -\frac{h_c}{2}\frac{\partial\theta}{\partial x} - (z_0 - \frac{h_c}{2})\frac{\partial^2 w}{\partial x^2}, \tag{4d}$$

where the strains along the x-axis for the top and bottom layers are denoted by ε_{tx} and ε_{bx}, respectively. The shear strain of the core layer is represented by γ_{cxz}^i, and the strain along the x-axis for the piezoelectric layer is denoted by ε_{px}.

The stress-strain relationship can be expressed as

$$\sigma_{tx} = E\left(-\frac{h_c}{2}\frac{\partial\theta}{\partial x} - \left(z_0 - \frac{h_c}{2}\right)\frac{\partial^2 w}{\partial x^2}\right), \tag{5a}$$

$$\tau_{cxz}^i = G_i\left(-\theta + \frac{\partial w}{\partial x}\right), \tag{5b}$$

$$\sigma_{bx} = E\left(\frac{h_c}{2}\frac{\partial\theta}{\partial x} - \left(z_0 + \frac{h_c}{2}\right)\frac{\partial^2 w}{\partial x^2}\right), \tag{5c}$$

$$\sigma_{px} = E_p\varepsilon_{px} - e_{31}E_1, \tag{5d}$$

where σ_{tx} and σ_{bx} represent the stresses along the x-axis in the top and bottom layers, respectively. The shear stress in the core layer is denoted by τ_{cxz}^i $(i = 1, 2)$, and the stress in the piezoelectric layer is denoted by σ_{px}.

The electric field E_1 is related to the output voltage $v(t)$ by the equation $E_1 = -v(t)/h_d$. For the piezoelectric layer, the Young's modulus is denoted by E_p, the piezoelectric constant by e_{31}, and the dielectric constant by ε_{33}.

The kinetic energy in the PDSB is expressed as

$$\begin{aligned} T = &\frac{1}{2}\int_{v_t}\rho_f((\dot{u}_t)^2 + (\dot{w}_a)^2)dV_t + \frac{1}{2}\int_{v_c}\rho_i^c((\dot{u}_c^i)^2 + (\dot{w}_c)^2)dV_c \\ &+ \frac{1}{2}\int_{v_b}\rho_f((\dot{u}_b)^2 + (\dot{w}_b)^2)dV_b + \frac{1}{2}\int_{v_p}\rho_p((\dot{u}_p)^2 + (\dot{w}_p)^2)dV_p, \end{aligned} \tag{6}$$

where V_t, V_c, and V_b represent the volumes of the top, core, bottom, and piezoelectric layers, respectively. Since the core layer of the sandwich beam is composed of trusses with varying radii, the kinetic energy of the core layer is calculated using a piecewise integration method as follows:

$$\begin{aligned} T_c = &\frac{1}{2}\int_{v_c}\rho_i^c((\dot{u}_c^i)^2 + (\dot{w}_c)^2)dV_c \\ = &\frac{1}{12}b\rho_i^c h_c^3\int_0^L\left(\frac{\partial\theta}{\partial t}\right)^2 dx + b\rho_i^c h_c\int_0^L\left(\frac{\partial w}{\partial t} + \frac{\partial w_c}{\partial t}\right)^2 dx \\ = &\frac{1}{12}bh_c^3\left(\int_0^{L_1}\rho_1^c\left(\frac{\partial\theta}{\partial t}\right)^2 dx + \int_{L_1}^{L_2}\rho_2^c\left(\frac{\partial\theta}{\partial t}\right)^2 dx + \cdots\right. \\ &\left. + \int_{L_{19}}^{L}\rho_2^c\left(\frac{\partial\theta}{\partial t}\right)^2 dx\right)bh_c\left(\int_0^{L_1}\rho_1^c\left(\frac{\partial w}{\partial t} + \frac{\partial w_c}{\partial t}\right)^2 dx\right. \\ &\left. + \int_{L_1}^{L_2}\rho_2^c\left(\frac{\partial w}{\partial t} + \frac{\partial w_c}{\partial t}\right)^2 dx + \cdots + \int_{L_{19}}^{L}\rho_2^c\left(\frac{\partial w}{\partial t} + \frac{\partial w_c}{\partial t}\right)^2 dx\right) \end{aligned} \tag{7}$$

The potential energy in the PDSB can be expressed as

$$\begin{aligned} U = &\frac{1}{2}\int_{v_t}\sigma_{tx}\varepsilon_{tx}dV_t + \frac{1}{2}\int_{v_c}\tau_{cxz}^i\gamma_{cxz}dV_c + \frac{1}{2}\int_{v_b}\sigma_{bx}\varepsilon_{bx}dV_b \\ &+ \frac{1}{2}\int_{v_p}\sigma_{px}\varepsilon_{px}dV_p. \end{aligned} \tag{8}$$

Similarly, the potential energy of the core layer can be calculated using the piecewise integration method, as given below:

$$\begin{aligned} U_c &= \frac{1}{2}\int_{v_c} \tau^i_{cxz}\gamma_{cxz}dV_c \\ &= G_i b h_c \int_0^L \left(\frac{\partial w}{\partial x}-\theta\right)^2 dx \\ &= bh_c\left(\int_0^{L_1} G_1\left(\frac{\partial w}{\partial x}-\theta\right)^2 dx + \int_{L_1}^{L_2} G_2\left(\frac{\partial w}{\partial x}-\theta\right)^2 dx \right. \\ &\quad \left. + \cdots + \int_{L_{19}}^{L_{20}} G_2\left(\frac{\partial w}{\partial x}-\theta\right)^2 dx\right) \end{aligned} \tag{9}$$

The electrical energy stored within the piezoelectric layer is expressed as

$$\begin{aligned} W_e &= \frac{1}{2}\int_{V_p} E_1(e_{31}\varepsilon_p + \varepsilon_{33}E_1)dV_p \\ &= \frac{1}{2}\int_0^{L_c}\left(J_{p1}v(t)\frac{\partial\theta}{\partial x} + J_{p2}v(t)\frac{\partial^2 w}{x^2}\right)dx + \frac{1}{2}C_p v^2(t) \end{aligned} \tag{10}$$

where $C_p = \varepsilon_{33} b L_p / h_d$ is the internal capacitance of the piezoelectric layer, the expressions for the coefficients J_{p1} and J_{p2} can be found in Appendix A.

2.3 Discretization of Energy Equations. The two components of the vibration response are expanded into a finite series of modal functions. For simplicity, it is assumed that the number of modal functions is identical for both components.

$$w(x,t) = \sum_{j=1}^{N} a_j(t)\varphi_j(x) = \boldsymbol{\varphi}^T(x)\boldsymbol{a}(t), \tag{11a}$$

$$\theta(x,t) = \sum_{j=1}^{N} c_j(t)\eta_j(x) = \boldsymbol{\eta}^{\mathrm{T}}(x)\boldsymbol{c}(t), \tag{11b}$$

where $\eta_j(x)$ and $\varphi_j(x)$ represent the modal shape functions that satisfy the boundary conditions, and $a_j(t)$ and $c_j(t)$ denote the unknown generalized coordinates. N refers to the number of modal shape functions used in the calculation.

The assumed mode for the n-order of a cantilever sandwich beam is given by:

$$\begin{aligned} \varphi_n(x) &= \cosh\left(k_n\frac{x}{L}\right) - \cos\left(k_n\frac{x}{L}\right) \\ &\quad - \frac{\sinh k_n - \sin k_n}{\cosh k_n + \cos k_n}\left[\sinh\left(k_n\frac{x}{L}\right) - \sin\left(k_n\frac{x}{L}\right)\right], \end{aligned} \tag{12a}$$

$$\begin{aligned} \eta_n(x) &= \sinh\left(k_n\frac{x}{L}\right) + \sin\left(k_n\frac{x}{L}\right) \\ &\quad - \frac{\sinh k_n - \sin k_n}{\cosh k_n + \cos k_n}\left[\cosh\left(k_n\frac{x}{L}\right) - \cos\left(k_n\frac{x}{L}\right)\right], \end{aligned} \tag{12b}$$

where the values of k_n for the first three modes of a cantilever sandwich beam are 1.875, 4.694, and 7.855, respectively [47,48]. For modes beyond the third ($n>3$), k_n can be expressed as $(n-0.5)\times\pi$.

By substituting Eqs. (11*a*) and (11*b*) into Eqs. (7), (8), and (10), the energies within the PDSB in the kinetic, potential, and electric forms can be discretized as follows:

$$\begin{aligned} T_1 &= \frac{1}{2}\sum_j^N\sum_e^N [\dot{a}_j(t)\dot{a}_e(t)m^{aa}_{je} + \dot{c}_j(t)\dot{c}_e(t)m^{cc}_{je} - 2\dot{a}_j(t)\dot{c}_j(t)m^{ac}_{je}] \\ &\quad + \frac{1}{2}\sum_j^N 2\dot{a}_j(t)p_j + \frac{1}{2}\int_0^L g^T_{11}\left(\frac{\partial w_c}{\partial x}\right)^2 dx, \end{aligned} \tag{13a}$$

$$\begin{aligned} U_1 &= \frac{1}{2}\sum_j^N\sum_e^N [a_j(t)a_e(t)k^{aa}_{je} + c_j(t)c_e(t)k^{cc}_{je} - 2a_j(t)c_j(t)k^{ac}_{je}] \\ &\quad - \frac{1}{2}\sum_j^N [c_j(t)v(t)\zeta^c_j - a_j(t)v(t)\zeta^a_j], \end{aligned} \tag{13b}$$

$$W_e = \frac{1}{2}\sum_j^N (a_j(t)v(t)\zeta^a_j + c_j(t)v(t)\zeta^c_j) + \frac{1}{2}C_p v^2(t), \tag{13c}$$

where the expressions for $\boldsymbol{\zeta}$ and $\mathbf{p}$ can be found in Appendix A.

Hamilton's principle was then applied to derive the motion governing equations of the diatomic sandwich beam as

$$\int_{t_1}^{t_2}[\delta(T-U)+\delta W]dt = 0, \tag{14}$$

where δW is the virtual work induced by the external force, T is the kinetic energy and U is the strain energy in the diatomic sandwich beam. The virtual work is given as

$$\delta W = F_1\delta w|_{x=x_0} = f\sin(\omega t)\delta w|_{x=x_0}, \tag{15}$$

where F_1 refers to the external force applied at the position of x_0 on the diatomic sandwich beam, and f and ω represent its amplitude and frequency, respectively.

Substituting Eqs. (6), (8), (11*a*), (11*b*), and (15) into Eq. (14), with the piezoelectric term in Eqs. (6) and (8) being temporarily omitted, the motion equation for the diatomic sandwich beam is obtained as follows:

$$\mathbf{M}\ddot{X}(t) + \mathbf{C}\dot{X}(t) + \mathbf{K}\mathbf{X}(t) = \mathbf{F}, \tag{16}$$

where $\mathbf{C}$ is the Rayleigh damping matrix, $\mathbf{M}$ is the mass matrix, and $\mathbf{K}$ is the stiffness matrix. The generalized coordinate vector $\mathbf{X}(t) = [a_j(t),\ c_j(t)]^T$ represents the transverse displacement and rotation angle, with further details provided in Appendix A.

2.4 Electromechanical Equations. Using Lagrange's equation, one can derive the governing equations of the PDSB [49]

$$\frac{d}{dt}\left(\frac{\partial T_1}{\partial\dot{a}_j(t)}\right) - \frac{\partial T_1}{\partial a_j(t)} + \frac{\partial U_1}{\partial a_j(t)} - \frac{\partial W_e}{\partial a_j(t)} = 0, \tag{17a}$$

$$\frac{d}{dt}\left(\frac{\partial T_1}{\partial\dot{c}_j(t)}\right) - \frac{\partial T_1}{\partial c_j(t)} + \frac{\partial U_1}{\partial c_j(t)} - \frac{\partial W_e}{\partial c_j(t)} = 0, \tag{17b}$$

$$\frac{d}{dt}\left(\frac{\partial T_1}{\partial\dot{v}_j(t)}\right) - \frac{\partial T_1}{\partial v_j(t)} + \frac{\partial U_1}{\partial v_j(t)} - \frac{\partial W_e}{\partial v_j(t)} = Q(t), \tag{17c}$$

where $j = 1, 2, \ldots, N$, and $Q(t)$ represents the charge accumulated in the internal capacitance of the piezoelectric layer. According to the relationships between charge, current, and voltage, one obtains:

$$\dot{Q}(t) = \frac{v(t)}{R}. \tag{18}$$

Substituting Eqs. (13*a*)–(13*c*) into Eqs. (17*a*)–(17*c*) yields

$$\sum_j^N (m^{aa}_{je}\ddot{a}_j(t) + m^{ac}_{je}\ddot{c}_j(t) + k^{aa}_{je}a_j(t) + k^{ac}_{je}c_j(t)) + \zeta^a_j v(t) = f_j, \tag{19a}$$

$$\sum_j^N (m^{ac}_{ej}\ddot{a}_j(t) + m^{cc}_{ej}\ddot{c}_j(t) + k^{ac}_{ej}a_j(t) + k^{cc}_{ej}c_j(t)) + \zeta^c_j v(t) = 0, \tag{19b}$$

$$C_p\dot{v}(t) + \frac{v(t)}{R} + \sum_j^N (\zeta^a_j\dot{a}_j(t) + \zeta^c_j\dot{c}_j(t)) = 0, \tag{19c}$$

where f_i is the force component generated by the base excitation. Furthermore, Eqs. (19*a*)–(19*c*) can be expressed in matrix form as

$$\mathbf{m}^{aa}\ddot{\mathbf{a}}(t) + \mathbf{m}^{ac}\ddot{\mathbf{c}}(t) + \mathbf{k}^{aa}\mathbf{a}(t) + \mathbf{k}^{ac}\mathbf{c}(t) + \boldsymbol{\zeta}^{a}v(t) = \mathbf{f}, \tag{20a}$$

$$(\mathbf{m}^{ac})^{T}\ddot{\mathbf{a}}(t) + \mathbf{m}^{cc}\ddot{\mathbf{c}}(t) + (\mathbf{k}^{ac})^{T}\mathbf{a}(t) + \mathbf{k}^{cc}\mathbf{c}(t) + \boldsymbol{\zeta}^{c}v(t) = 0, \tag{20b}$$

$$C_p\dot{v}(t) + \frac{v(t)}{R} + (\boldsymbol{\zeta}^{a})^{T}\dot{a}_j(t) + (\boldsymbol{\zeta}^{c})^{T}\dot{c}_j(t) = 0, \tag{20c}$$

where

$$\begin{cases} \mathbf{a} = [a_1, a_2, ..a_N]^T, \mathbf{c} = [c_1, c_2, ..c_N]^T, \mathbf{f} = [f_1, f_2, ..f_N]^T, \\ \boldsymbol{\zeta}^{a} = [\zeta_1^{a}, \zeta_2^{a}, ..\zeta_N^{a}]^T, \boldsymbol{\zeta}^{c} = [\zeta_1^{c}, \zeta_2^{c}, ..\zeta_N^{c}]^T. \end{cases} \tag{21}$$

Equations (20a)–(20c) can be further rewritten as:

$$\begin{bmatrix} \mathbf{m}^{aa} & \mathbf{m}^{ac} \\ (\mathbf{m}^{ac})^{T} & \mathbf{m}^{cc} \end{bmatrix}\begin{bmatrix} \ddot{\mathbf{a}}(t) \\ \ddot{\mathbf{c}}(t) \end{bmatrix} + \begin{bmatrix} \mathbf{k}^{aa} & \mathbf{k}^{ac} \\ (\mathbf{k}^{ac})^{T} & \mathbf{k}^{cc} \end{bmatrix}\begin{bmatrix} \mathbf{a}(t) \\ \mathbf{c}(t) \end{bmatrix} + \begin{bmatrix} \boldsymbol{\zeta}^{a} \\ \boldsymbol{\zeta}^{c} \end{bmatrix}v(t) = \begin{bmatrix} \mathbf{f} \\ 0 \end{bmatrix}. \tag{22}$$

Typically, Rayleigh damping is used to characterize the energy dissipation in the structure, and its expression is given by:

$$\begin{bmatrix} \mathbf{C}^{aa} & \mathbf{C}^{ac} \\ (\mathbf{C}^{ac})^{T} & \mathbf{C}^{cc} \end{bmatrix} = \alpha\begin{bmatrix} \mathbf{m}^{aa} & \mathbf{m}^{ac} \\ (\mathbf{m}^{ac})^{T} & \mathbf{m}^{cc} \end{bmatrix} + \beta\begin{bmatrix} \mathbf{k}^{aa} & \mathbf{k}^{ac} \\ (\mathbf{k}^{ac})^{T} & \mathbf{k}^{cc} \end{bmatrix}. \tag{23}$$

Specifically, α and β represent the mass and stiffness proportional damping coefficients in the Rayleigh damping model. Their values were determined by matching the target modal damping ratios for the first and second vibration modes of the PDSB, following the standard relations: $\alpha = \dfrac{2\omega_1\omega_2(\xi_1\omega_2 - \xi_2\omega_1)}{\omega_2^2 - \omega_1^2}$, $\beta = \dfrac{2(\xi_2 - \xi_1)}{\omega_2^2 - \omega_1^2}$. Where ω_1 and ω_2 are the natural angular frequencies of the first and second modes, and ξ_1 and ξ_2 are the corresponding damping ratios. In our simulations, we set $\xi_1 = \xi_2 = 1\%$.

Thus, Eq. (22) can be expanded as

$$\begin{bmatrix} \mathbf{m}^{aa} & \mathbf{m}^{ac} \\ (\mathbf{m}^{ac})^{T} & \mathbf{m}^{cc} \end{bmatrix}\begin{bmatrix} \ddot{\mathbf{a}}(t) \\ \ddot{\mathbf{c}}(t) \end{bmatrix} + \begin{bmatrix} \mathbf{c}^{aa} & \mathbf{c}^{ac} \\ (\mathbf{c}^{ac})^{T} & \mathbf{c}^{cc} \end{bmatrix}\begin{bmatrix} \dot{\mathbf{a}}(t) \\ \dot{\mathbf{c}}(t) \end{bmatrix} \times \begin{bmatrix} \mathbf{k}^{aa} & \mathbf{k}^{ac} \\ (\mathbf{k}^{ac})^{T} & \mathbf{k}^{cc} \end{bmatrix}\begin{bmatrix} \mathbf{a}(t) \\ \mathbf{c}(t) \end{bmatrix} + \begin{bmatrix} \boldsymbol{\zeta}^{a} \\ \boldsymbol{\zeta}^{c} \end{bmatrix}v(t) = \begin{bmatrix} \mathbf{f} \\ 0 \end{bmatrix}, \tag{24}$$

It is worth noting that the submatrices for mass, stiffness and damping are all $N \times N$ matrices.

2.5 Frequency-Domain Response. This section considers harmonic excitation for frequency-domain analysis, while the general time-domain equations (Eq. (24)) remain applicable to an arbitrary base excitation $g(t)$ and $\theta_a(t)$ and can be solved numerically. For harmonic analysis, the base excitation can be expressed in the following form:

$$w_c(x, t) = W_0 e^{j\omega t} + \theta_0 e^{j\omega t}, \tag{25}$$

The external excitation f_j can be expressed as

$$f_j = F_j \sin(\omega t), \tag{26}$$

where

$$F_j = (W_0\int_0^{L_p} g_{11}^{T}\varphi_j(x)dx + \theta_0\int_0^{L_p} g_{11}^{T}\varphi_j(x)xdx)\omega^2. \tag{27}$$

The general solutions for the generalized coordinates and voltage output are assumed as

$$\mathbf{a} = \mathbf{A}e^{j\omega t}, \mathbf{c} = \mathbf{C}e^{j\omega t}, v = Ve^{j\omega t}, \tag{28}$$

where $\mathbf{A}$, $\mathbf{C}$, and V are complex vectors/numbers.

The voltage V can be represented by $\mathbf{A}$ and $\mathbf{C}$ by solving Eq. (20c):

$$V = j\omega[(\boldsymbol{\zeta}^{a})^{T}\mathbf{A} + (\boldsymbol{\zeta}^{c})^{T}\mathbf{C}](j\omega C_p + \frac{1}{R})^{-1}, \tag{29}$$

or alternatively,

$$v = [(\boldsymbol{\zeta}^{a})^{T}\dot{\mathbf{a}}(t) + (\boldsymbol{\zeta}^{c})^{T}\dot{\mathbf{c}}(t)](j\omega C_p + \frac{1}{R})^{-1}. \tag{30}$$

Multiplying both sides of Eq. (3) by an identical column vector gives:

$$\begin{aligned} \begin{bmatrix} \boldsymbol{\zeta}^{a} \\ \boldsymbol{\zeta}^{c} \end{bmatrix}v(t) &= \left(j\omega C_p + \frac{1}{R}\right)^{-1}\begin{bmatrix} \boldsymbol{\zeta}^{a} \\ \boldsymbol{\zeta}^{c} \end{bmatrix}\begin{bmatrix} (\boldsymbol{\zeta}^{a})^{T} & (\boldsymbol{\zeta}^{c})^{T} \end{bmatrix}\begin{bmatrix} \dot{\mathbf{a}}(t) \\ \dot{\mathbf{c}}(t) \end{bmatrix} \\ &= \left(j\omega C_p + \frac{1}{R}\right)^{-1}\begin{bmatrix} \boldsymbol{\zeta}^{a}(\boldsymbol{\zeta}^{a})^{T} & \boldsymbol{\zeta}^{a}\boldsymbol{\zeta}^{c} \\ \boldsymbol{\zeta}^{c}(\boldsymbol{\zeta}^{a})^{T} & \boldsymbol{\zeta}^{c}(\boldsymbol{\zeta}^{c})^{T} \end{bmatrix}\begin{bmatrix} \dot{\mathbf{a}}(t) \\ \dot{\mathbf{c}}(t) \end{bmatrix}. \end{aligned} \tag{31}$$

By substituting Eqs. (28)–(31) into Eq. (24), we obtain:

$$\begin{bmatrix} \boldsymbol{\varsigma}^{a}(\boldsymbol{\varsigma}^{a})^{T} & \boldsymbol{\varsigma}^{ac}(\boldsymbol{\varsigma}^{ac})^{T} \\ (\boldsymbol{\varsigma}^{ac})^{T}\boldsymbol{\varsigma}^{ac} & \boldsymbol{\varsigma}^{c}(\boldsymbol{\varsigma}^{c})^{T} \end{bmatrix}\begin{bmatrix} \mathbf{A} \\ \mathbf{C} \end{bmatrix} = \begin{bmatrix} \mathbf{F} \\ 0 \end{bmatrix}. \tag{32}$$

The specific expression for the mechanical impedance matrix is provided in Appendix B. The generalized coordinates can then be derived by solving Eq. (32).

$$\begin{bmatrix} \mathbf{A} \\ \mathbf{C} \end{bmatrix} = \begin{bmatrix} \boldsymbol{\varsigma}^{a}(\boldsymbol{\varsigma}^{a})^{T} & \boldsymbol{\varsigma}^{a}\boldsymbol{\varsigma}^{c} \\ \boldsymbol{\varsigma}^{c}(\boldsymbol{\varsigma}^{a})^{T} & \boldsymbol{\varsigma}^{c}(\boldsymbol{\varsigma}^{c})^{T} \end{bmatrix}^{-1}\begin{bmatrix} \mathbf{F} \\ 0 \end{bmatrix}. \tag{33}$$

Finally, the electromechanical coupling equations are established as follows:

$$\mathbf{M_1}\ddot{\mathbf{X}}(t) + \mathbf{C}\dot{\mathbf{X}}(t) + \mathbf{K_1}\mathbf{X}(t) + \begin{bmatrix} \boldsymbol{\zeta}^{a} \\ \boldsymbol{\zeta}^{c} \end{bmatrix}v(t) = \mathbf{f}, \tag{34}$$

$$C_p\dot{v}(t) + \frac{v(t)}{R} + [(\boldsymbol{\zeta}^{a})^{T}, (\boldsymbol{\zeta}^{c})^{T}]\dot{\mathbf{X}}(t) = 0, \tag{35}$$

where $\mathbf{C}$ represents the Rayleigh damping matrix, $\mathbf{M_1}$ and $\mathbf{K_1}$ are the mass and stiffness matrices of the PDSB, with their detailed expressions provided in Appendix C. The voltage generated by the piezoelectric patch can be derived by solving Eqs. (34) and (35) simultaneously.

3 Numerical Results and Discussions

In this section, simulations are performed to systematically investigate the dynamics and energy harvesting characteristics of the PDSB. The finite element (FE) simulation results are compared with the theoretical predictions to verify the accuracy and reliability of the developed theoretical model. In addition, the effects of geometric and material parameters, such as Young's modulus, strut radii, layer thickness, etc., on the structural dynamics and energy harvesting performance are discussed to provide insights for optimization.

3.1 Model Verification. The natural frequencies of the PDSB under the clamped-free boundary condition were calculated using COMSOL Multiphysics software. The geometric and material parameters of the PDSB under investigation are listed in Table 1.

The first five natural frequencies of the PDSB, with the parameters listed in Table 1, were also calculated using the proposed method and compared with the FE results, as listed in Table 2. The relative errors between the two results were found to be acceptably within 5%. It is worth mentioning that the model examined here corresponds to the PDSB without the piezoelectric material.

Table 1 Geometric and material parameters of the proposed PDSB [50]

Symbol	Value	Unit
L	2	m
E	200	Gpa
E_p	66	Gpa
b	0.05	m
h_f	0.01	m
h_c	0.05	m
r_1	0.005	m
r_2	0.003	m
L_p	0.2	m
h_d	0.002	m
ρ_p	7500	kg/m^3
ρ_f	7850	kg/m^3
R	1×106	Ω
e_{31}	−12.54	C m^{-2}
ε_{33}	15.93	nF m^{-1}

Table 2 First five natural frequencies (Hz) of the cantilevered PDSB

Modes	FEM	Present method	Relative error (%)
1	19.255	18.585	3.47
2	108.33	110.30	1.78
3	266.19	286.63	2.55
4	451.99	442.21	2.16
5	650.32	639.93	1.59

Table 3 Convergence analysis for the modal order (unit: Hz)

Modes	1	2	3	6
First natural frequency	18.742	18.582	18.585	18.585
Voltage output	12.885	12.754	12.734	12.732

To determine the appropriate number of mode shapes and electromechanical coupling modes, a convergence verification study was conducted, with the results listed in Table 3. The results show that the structural natural frequency and voltage output converge when the first three mode shapes are considered. Therefore, the first three mode shapes will be included in the calculation in subsequent studies.

Figures 4 and 5 demonstrate the first four mode shapes of the PDSB, calculated using FE simulation and the proposed theoretical method, respectively. The good agreement between the theoretical predictions and FE results confirms the accuracy of the developed theoretical model.

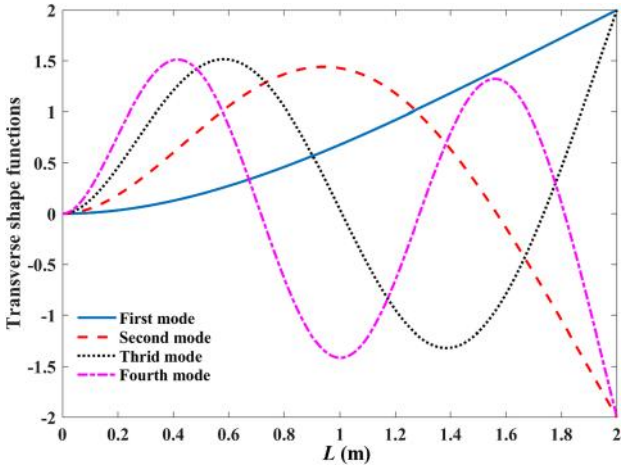

Fig. 5 The first four modes of the PDSB obtained by the developed theoretical method

3.2 Energy Harvesting Performance Evaluation. This section analyzes the energy harvesting performance of the PDSB. Prior to this, a convergence analysis of the dynamic characteristics of its homogenized FE model, as shown in Fig. 6, was conducted. In the corresponding homogenized FE model, the core layer is modeled as an equivalent homogeneous soft medium to better align with the theoretical model. Table 4 clearly shows that refining the mesh by increasing the number of elements leads to convergence of the first two natural frequencies. Therefore, a 40×4 mesh model was used in the FE modeling of the PDSB.

Figure 7 illustrates the displacement and voltage responses of the PDSB under an external excitation with a force of 1 N. As shown in Figs. 7(*a*) and 7(*b*), the maximum relative errors between theoretical and FE results for the resonant frequency and voltage amplitude were 3.47% and 0.39%, respectively, within the acceptable error margin from an engineering perspective. The discrepancy primarily stems from the homogenization of the core layer, which simplifies the hourglass-shaped core structure [18,19]. Nevertheless, the results have basically proven the accuracy of the theoretical model in predicting the energy harvesting performance of the PDSB.

To verify the superior energy harvesting performance of the PDSB structure, a comparison with a traditional piezoelectric uniform beam was conducted, with the results shown in Fig. 8. It is worth mentioning that the length and width of the uniform beam were intentionally tuned to be the same as those of the PDSB, while its thickness was set to 0.09 m to make sure it has

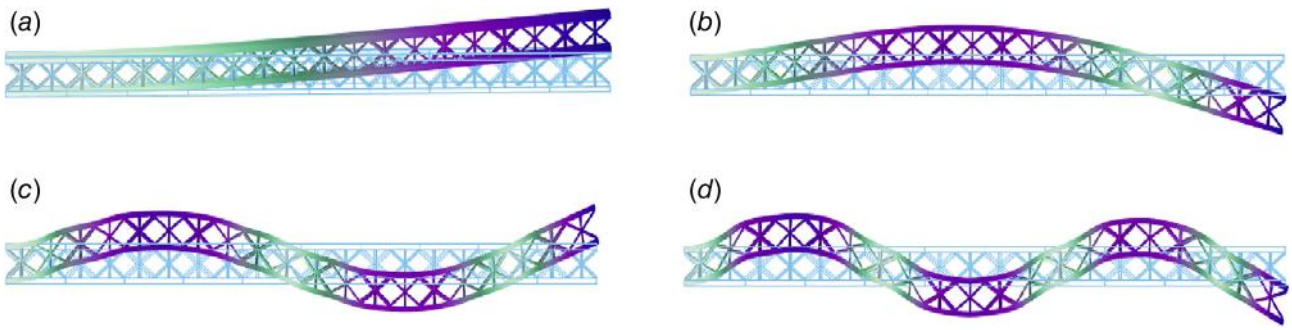

Fig. 4 The first four modes of the PDSB obtained by FE simulation: (*a*) the first-mode shape; (*b*) the second-mode shape; (c) the third-mode shape; and (*d*) the fourth-mode shape

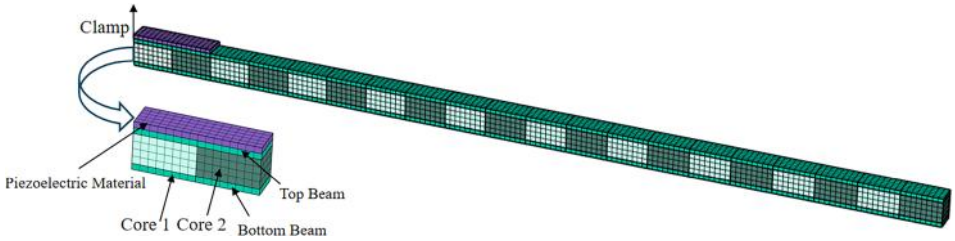

Fig. 6 Homogenized finite element model of the PDSB

Table 4 Mesh convergence analysis for the homogenized FE model of the PDSB

Meshing	10 × 4	20 × 4	30 × 4	40 × 4
First natural frequency	19.256	19.255	19.255	19.255
Second natural frequency	108.35	108.34	108.33	108.33

the same equivalent bending stiffness as well [51]. As illustrated in Fig. 8(*a*), the voltage output of the PDSB is 2.67 times higher than that of the uniform beam, and it exhibits a wider operation bandwidth, showing higher efficiency and adaptability for energy harvesting. Additionally, the power output of the PDSB significantly outperforms that of the uniform beam, with a capacity 7.14 times greater, as shown in Fig. 8(*b*). In summary, the PDSB exhibits

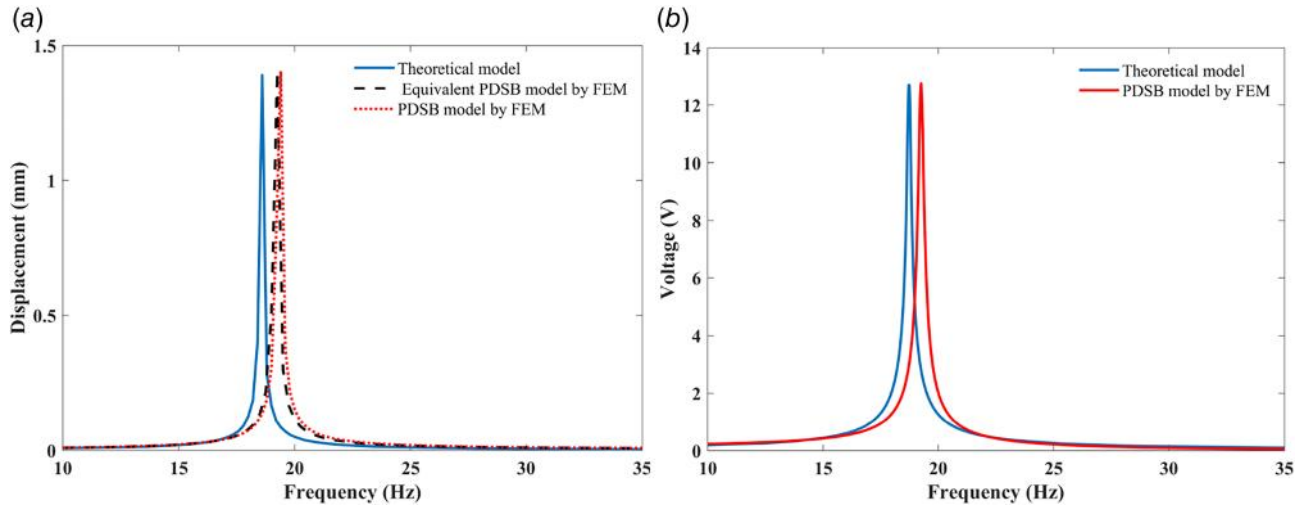

Fig. 7 (*a*) Displacement response; (*b*) voltage output of the PDSB calculated by the theory and FEM

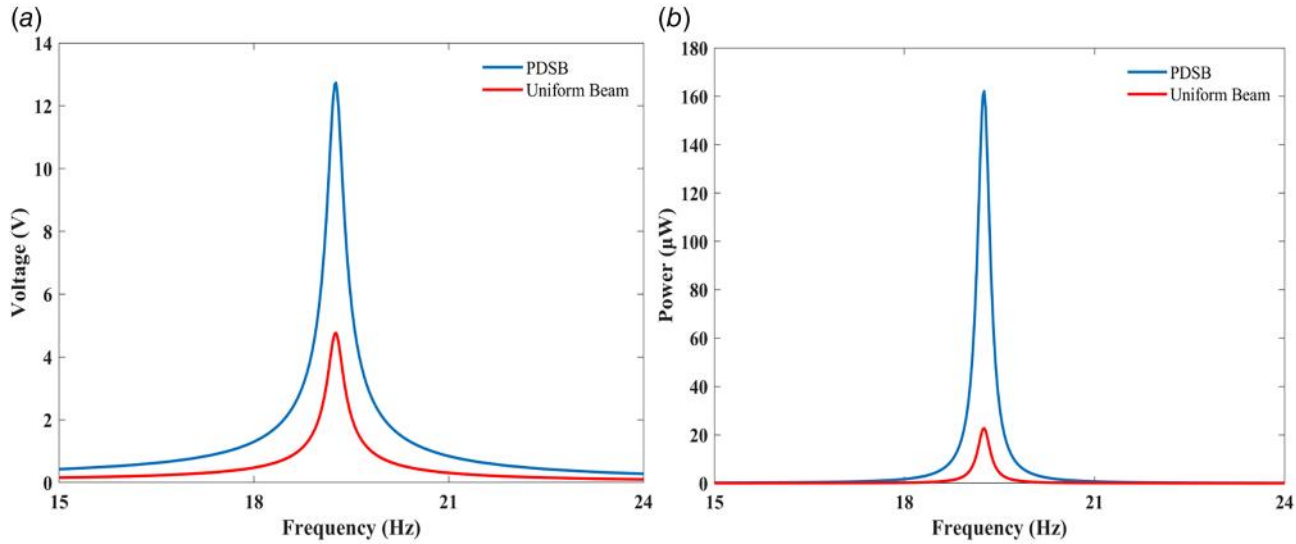

Fig. 8 Comparison of the energy harvesting performance between the PDSB and a uniform beam with identical length, width, and bending stiffness: (*a*) voltage output; (*b*) power output

superior performance over a uniform piezoelectric beam in terms of the open-circuit voltage, power, and operational bandwidth. In particular, its broadband characteristic makes it suitable for energy harvesting in practical scenarios where frequency fluctuations are common.

3.3 Effects of Geometric and Material Parameters. This section provides a detailed analysis of the effects of various parameters on the voltage and power outputs of the PDSB using the theoretical model. For simplicity, when one parameter is varied, the others remain constant. Figure 9 shows the voltage output of the PDSB with different Young's modulus E (100 GPa, 200 GPa, 300 GPa, and 450 GPa). It can be observed that with the increase of E, the structural resonant frequency increases, while the voltage output decreases. This is because an increase in Young's modulus enhances the structural stiffness, thereby increasing the resonant frequency. On the other hand, since the output voltage is proportional to strain, the reduced strain in materials with a larger Young's modulus results in a lower output voltage.

Figure 10 shows that increasing r_2 causes the PDSB resonant frequency to decrease. This is due to the fact that in complex structures such as sandwich beams, the mass increase resulting from changes in the radius has a more complicated effect on the overall dynamic characteristics [52]. Rather than simply increasing stiffness, the mass redistribution and the updated coupling between model components lead to a reduction in the natural frequency, reflecting a dynamic tradeoff between stiffness and mass. It is worth noting that the change in r_2 has little effect on the maximum output voltage amplitude.

Figure 11 demonstrates that as h_c increases from 30 mm to 60 mm, the resonant frequency gradually increases from 13.23 Hz to 21.31 Hz. This is because the increase in thickness alters the equivalent stiffness and mass distribution. A thicker core layer significantly enhances the bending stiffness of the beam, thereby increasing the natural frequency of the PDSB. The peak open-circuit voltage decreases slowly with the increase of h_c (from 13.36 V at 30 mm to 12.57 V at 60 mm). This is due to the fact that as h_c increases, the total strain energy of the PDSB gets more concentrated in the core layer, and the strain in the piezoelectric layer decreases, thus the voltage output induced by the piezoelectric effect decreases. The above results suggest that soft materials with lower stiffness should be selected for the core to maximize the voltage output of the PDSB.

Figure 12 shows that if the thicknesses of the top and bottom layers, i.e., h_t and h_b, are the same and increase simultaneously, the resonant frequency of the PDSB increases significantly. In the meantime, the output voltage drops rapidly. When the thicknesses of the top and bottom layers are different, the output voltage rapidly decreases with the increase of the h_b, and slowly decreases with the increase of h_t. This phenomenon results from the asymmetry of the structure of the PDSB [53]. Overall, varying the thicknesses of the top and bottom layers provides greater flexibility in the design of the PDSB.

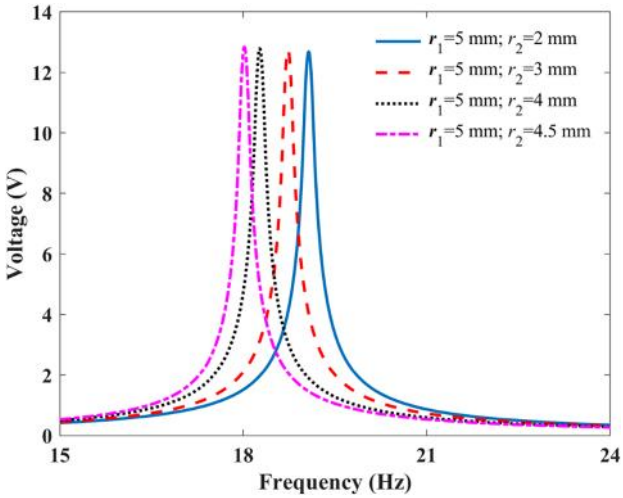

Fig. 10 Effect of r_1 and r_2 on voltage output of the PDSB

Figure 13 shows the voltage output of the PDSB when using materials with different densities. The density of common plastics and rubbers ranges between 800 kg/m^3 and 1500 kg/m^3, while some metal materials have densities between 7000 kg/m^3 and 8000 kg/m^3. The results reveal that when the structural material is plastic and rubber with a low mass density, the equivalent density of the core layer differs significantly compared to metal materials with high densities. This difference has a great impact on the energy harvesting performance. Counterintuitively, PDSBs with core layers made of soft plastics or rubbers require higher frequencies to achieve resonance, causing energy to distribute over a broader frequency range, which results in a lower voltage peak. In contrast, using metals can achieve resonance at low frequencies, concentrating energy in a narrower frequency range, which leads to a higher output voltage peak.

3.4 Effect of Load Resistance. This section explores the effect of the load resistor R on the energy harvesting performance of the PDSB. Except for the load resistor R, other system parameters remain the same as those listed in Table 1. Figure 14 shows that

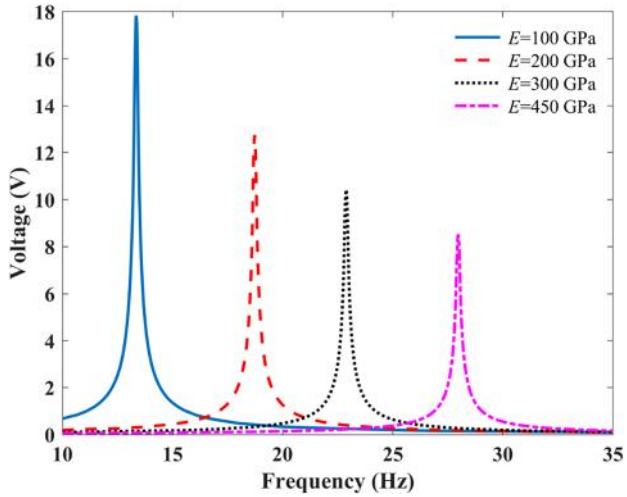

Fig. 9 Effect of E on the output voltage of the PDSB

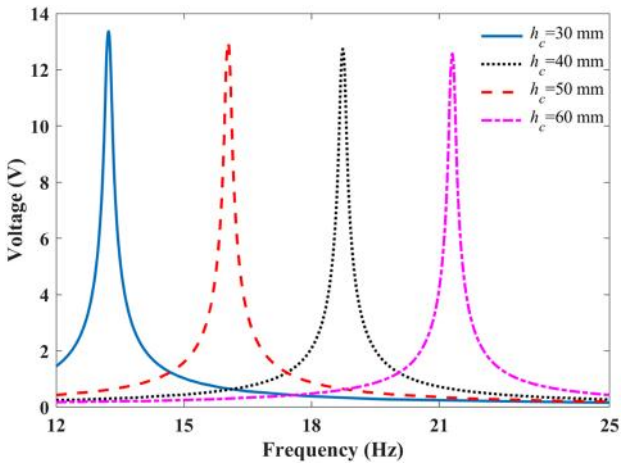

Fig. 11 Effect of h_c on voltage output of the PDSB

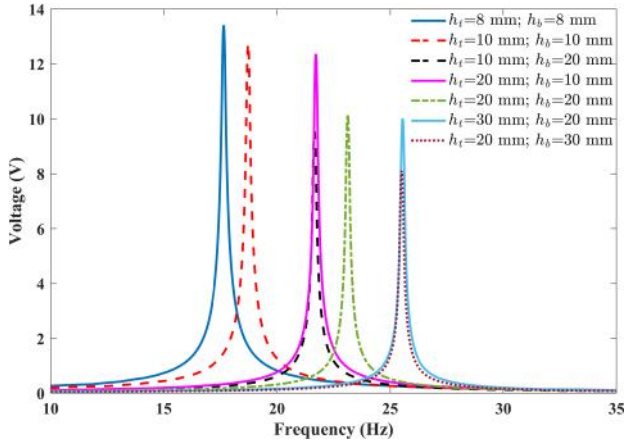

Fig. 12 Effect of different h_t and h_b thicknesses on the voltage output of the PDSB

changing R will affect the voltage and power outputs of the PDSB. The outputs reach peak values at the PDSB resonant frequency of 18.73 Hz, reflecting the inherent vibration characteristics, with the frequency response exhibiting evident narrow-band behavior. In Fig. 14(*a*), one notes that as R increases, the output voltage peak gradually rises, eventually saturating and approaching the open-circuit voltage amplitude. In Fig. 14(*b*), when R is tuned to the optimal, the energy harvester efficiency is maximized, and the power output attains the maximum.

Figure 15 shows the variation of the power output with different R at a frequency of 18.73 Hz. As R increases, the power output first increases and then decreases, with a maximum power of 0.744 mW obtained at approximately 100 kΩ. Therefore, to maximize the power output, the optimal load resistance must be selected according to the impedance matching theory. To further evaluate the performance of the PDSB under different external excitations, additional power output analyses are performed using the optimal load resistance. The results are shown in Fig. 16. The generated power is 0.744 mW, 3.01 mW, and 6.79 mW for external

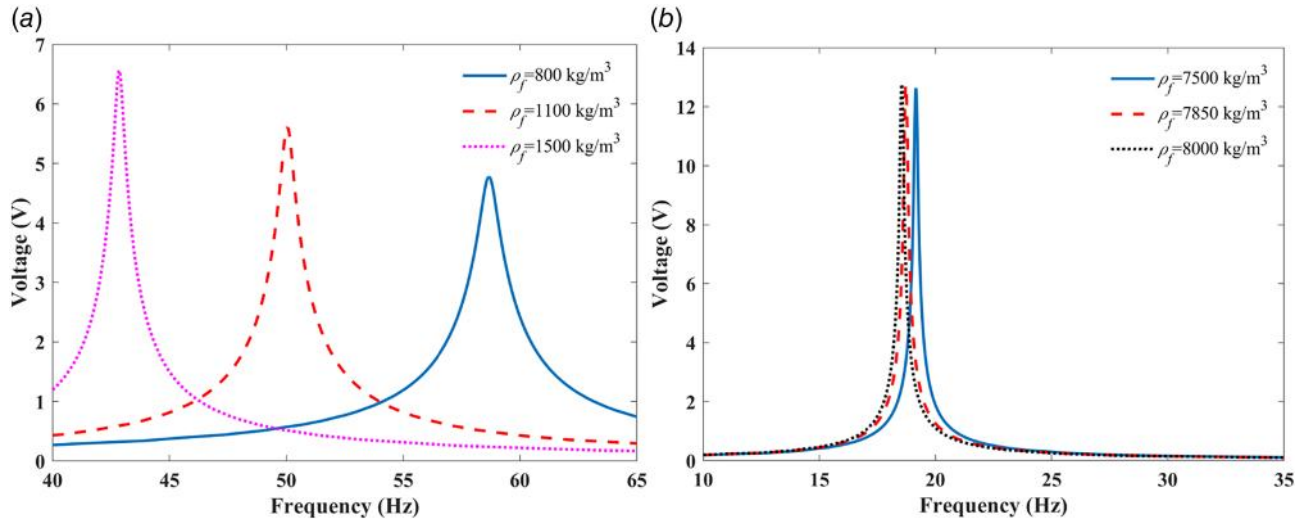

Fig. 13 Effect of material density on output voltage of the PDSB: (*a*) soft plastic and rubber materials; (*b*) metal materials

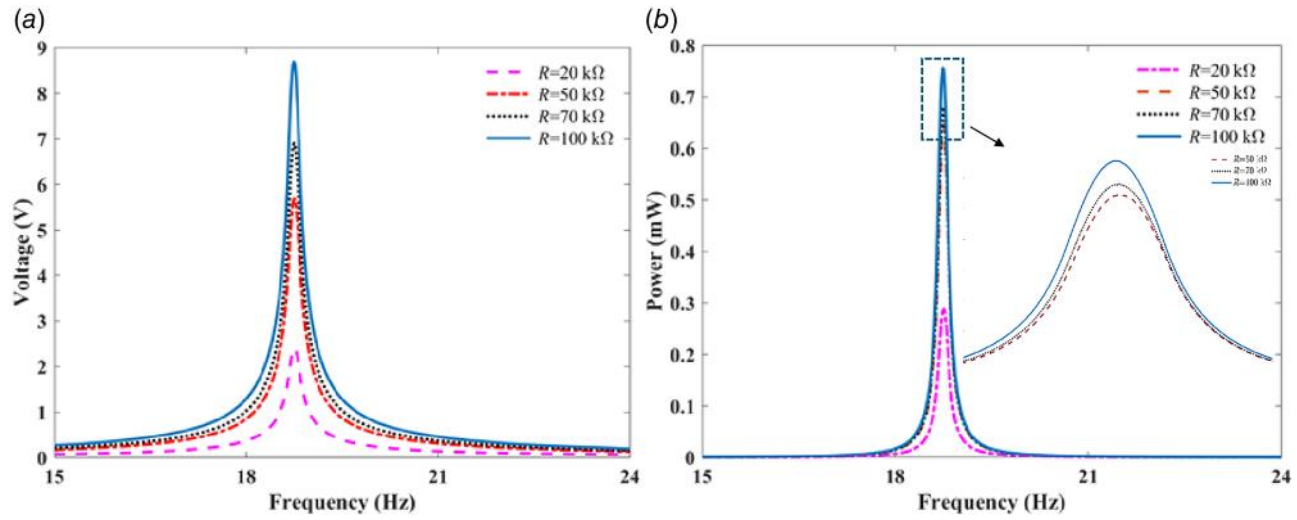

Fig. 14 Effect of resistive load on (*a*) output voltage; (*b*) power output

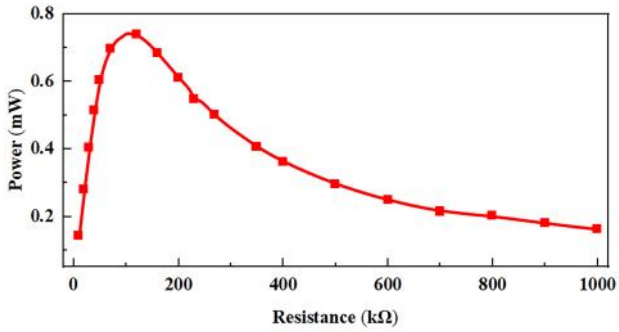

Fig. 15 Power output at the frequency of 18.73 Hz for different load resistances

excitations of 1 N, 2 N, and 3 N, respectively. The PDSB uses the piezoelectric effect to convert mechanical energy into electricity, and the power output is positively correlated with the applied excitation force. Therefore, as the applied force increases, the power output also rises.

4 Interface Circuit Analysis

This section introduces the equivalent circuit model (ECM) of the PDSB, along with a more advanced SECE circuit designed to enhance efficiency. The traditional RS circuit serves as a benchmark for comparison. The SECE circuit demonstrated in this section offers superior efficiency and stability across a wide impedance range, significantly boosting both power output and voltage stability.

4.1 Equivalent Circuit Model of PDSB. The governing equations of the PDSB in Eqs. (34) and (35) are first converted into modal form as [44]

$$\ddot{q}_n(t) + 2\xi_n\omega_n\dot{q}_n(t) + \omega_n^2 q_n(t) + \varepsilon_n v(t) = f_n, \tag{36}$$

$$C_p\dot{v}(t) + \frac{v(t)}{R} + \sum_{n=1}^{N}\varepsilon_n\dot{q}_n(t) = 0, \tag{37}$$

where the over-dot indicates the time derivative, ξ_n and ω_n are the modal damping ratio and the natural frequency under open-circuit conditions of the n-order vibration mode, respectively, and ε_n is the modal electromechanical coupling coefficient. Equations (36) and

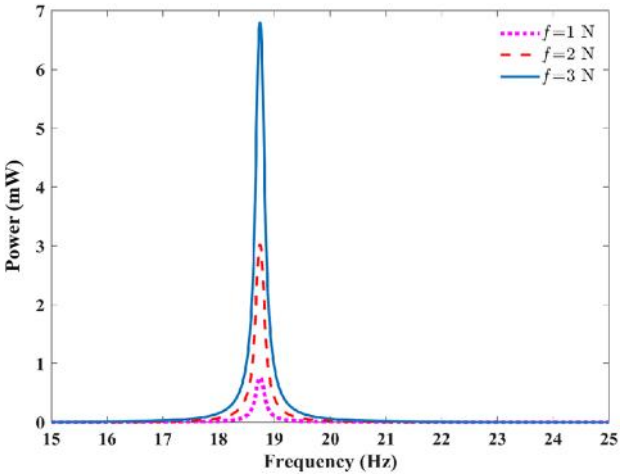

Fig. 16 Power output of the PDSB under different base excitations of 1 N, 2 N, and 3 N, with $R = 100$ k

Table 5 Analogies between mechanical and electrical quantities [40]

Mechanical	Electrical
$q_n(t)$	Charge, Q_n
$dq_n(t)/dt$	Current, I_n
Modal mass, 1	Inductance, L_n
$2\xi_n\omega_n$	Resistance, R_n
$1/\omega_n^2$	Capacitance, C_n
f_n	Voltage source, V
ε_n	Transformer ratio, T_n

(37) can be rewritten in matrix and vector form as

$$\begin{bmatrix}\mathbf{M}_2 & 0\\ 0 & 0\end{bmatrix}\begin{bmatrix}\ddot{\mathbf{q}}\\ \ddot{\mathbf{v}}\end{bmatrix} + \begin{bmatrix}\mathbf{C}_1 & 0\\ \varepsilon_n & \mathbf{C}_p\end{bmatrix}\begin{bmatrix}\dot{\mathbf{q}}\\ \dot{\mathbf{v}}\end{bmatrix} + \begin{bmatrix}\mathbf{K}_2 & \varepsilon_n\\ 0 & \dfrac{1}{R}\end{bmatrix} = \begin{bmatrix}\mathbf{f}_n\\ 0\end{bmatrix}, \tag{38}$$

where $\mathbf{M}_2$ is the $N \times N$ identity matrix, $\mathbf{q} = [q_1, q_2, \ldots, q_n]^T$, $\mathbf{C}_1 = 2 \times \text{diag}(\xi_1\omega_1, \xi_2\omega_2, \ldots, \xi_n\omega_n)$, $\mathbf{K}_2 = \text{diag}(\omega_1^2, \omega_2^2, \ldots, \omega_n^2)$, $\boldsymbol{\varepsilon}_\mathbf{n} = [\varepsilon_1, \varepsilon_2, \ldots, \varepsilon_n]^T$, $\mathbf{f_n} = [f_1, f_2, \ldots, f_n]^T$. The initial conditions are set as follows

$$q_n(0) = 0, \quad \dot{q}_n(0) = 0, \quad v(0) = 0. \tag{39}$$

Table 5 illustrates the analogies between the mechanical and electrical quantities, allowing the governing equations of the system (Eqs. (34) and (35)) to be transformed into the form of circuit governing equations. Figure 17 presents the established ECM of the PDSB connected to a simple load resistor. This circuit model can be easily implemented in any circuit simulation software, such as SIMetrix. The load resistance can be replaced with any other complicated shunt circuit, facilitating a comprehensive evaluation of the PDSB's energy harvesting performance.

The equivalent circuit model shown in Fig. 17 consists of six independent loops, each representing a vibration mode of the PDSB. The corresponding equivalent electrical parameters are listed in Table 6. To verify the ECM, circuit simulations were conducted, and the results were compared with the theoretical results, as shown in Fig. 18 for a purely resistive load of $R = 1000$ kΩ. The results demonstrate excellent consistency. In the following section, the ECM is shunted to an advanced SECE circuit, and a system-level analysis of the energy harvesting performance of the PDSB is performed.

4.2 SECE Control Strategy. Improving the power output of an energy harvester can be achieved not only through structural optimization but also by utilizing advanced power-boosting interface circuits [44,54,55]. Among these, the SECE circuit is one of the most widely used, and its schematic is shown in Fig. 19. To focus on the SECE circuit, the energy harvester is represented as a current source for simplicity. Switch S_1 remains open until the voltage V_1 across the piezoelectric transducer reaches its peak. At that instant, switch S_1 immediately closes, transferring the energy stored in capacitor C_1 to inductor L_1. Once the first phase of transfer is complete, the switch reopens, and the energy in L_1 begins to be transferred to capacitor C_2, initiating the second phase of transfer. This process then repeats cyclically. Numerous studies have demonstrated that this circuit can effectively improve energy conversion efficiency, boost power output, and resolve resistance-matching issues [56,57].

Similarly, Fig. 20 shows a self-powered SECE (SP-SECE) circuit for a piezoelectric energy harvesting (PEH). Before the PEH's voltage output reaches its peak, the rectified current charges capacitor C_2. During this period, both transistors Q_1 and Q_2 remain nonconducting. When the voltage across C_1 reaches its peak, the voltage across C_2 exceeds that across C_1, causing reverse current to flow into the emitter of Q_1. This triggers both transistors (Q_1 and Q_2) to turn on, transferring the energy stored in C_1 to inductor

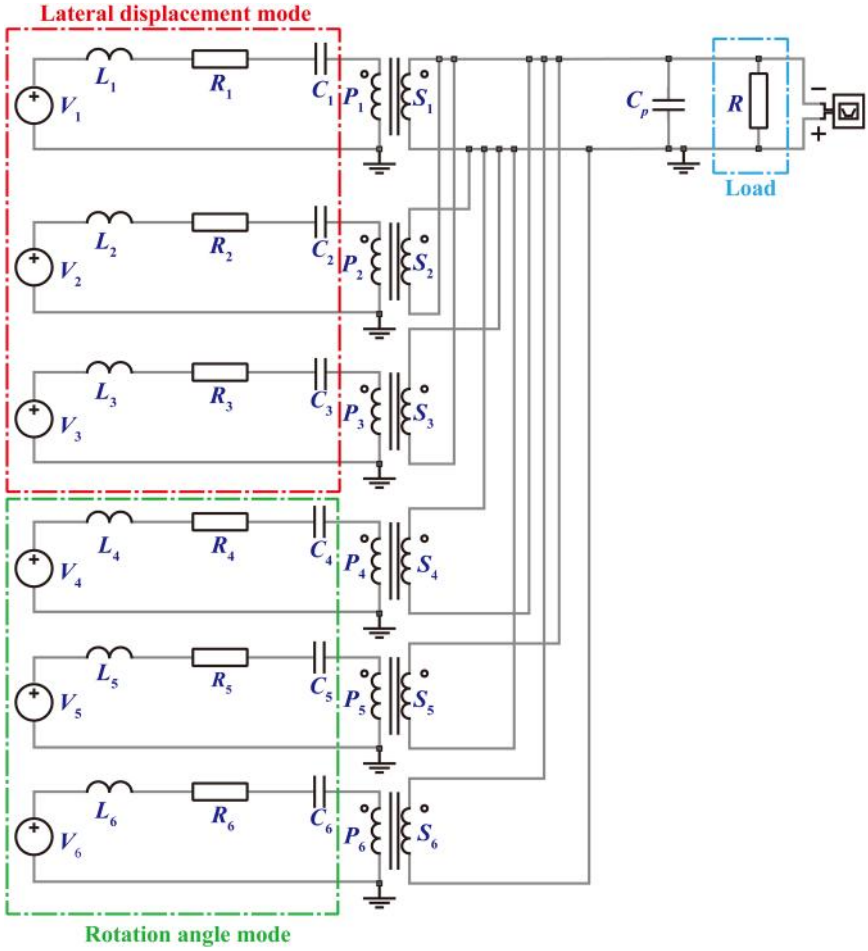

Fig. 17 Circuit representation of the PDSB connected to a resistive shunt (RS) circuit

Table 6 Equivalent electrical parameters of the first six modes of the PDSB

n	L_n (H)	C_n (F)	R_n (Ω)	T_n	V
1	1	13,886.13	4.712	625	0.3607
2	1	4,91,354.11	28.03	133.33	−0.3634
3	1	33,98,742.33	73.74	69.9301	−0.3513
4	1	138,59,22,615.39	1489.1	34.4828	−0.0049
5	1	151,64,90,664.99	1557.7	10.1112	−0.0038
6	1	178,55,73,882.46	1690.2	4.3917	−0.0295

L_1. After the energy transfer is complete, the transistors automatically turn off, and L_1 begins to supply power to capacitor C_3 and load R_4. In the following study, the PEH is replaced by the ECM of the PDSB to verify the improvements in the output power and energy efficiency brought by the SECE circuit.

4.3 SECE Circuit Integration. The circuit model of the system was established in SIMetrix, including the SECE circuit, as shown in Fig. 21. It mainly consists of three parts: the ECM of the PDSB, the piezoelectric transducer, and the SECE circuit. The ECM of the PDSB is represented by multiple independent circuit loops on the left-hand side. The piezoelectric transducer is equivalent to the combination of a series of transformers and an internal capacitance. The SECE circuit is implemented using a self-powered strategy. It uses an electronic circuit breaker composed of an envelope detector and a comparator. In the simulation, all diodes (D_1 to D_9) were modeled as ideal components, and transistors Q_1 and Q_2 use the 2N2904 and 2N2222 models provided in SIMetrix's built-in library, respectively. An inductor of 470 μH was selected to form an LC oscillation with the piezoelectric capacitor (79.65 nF) for instantaneous energy extraction. The values of C_8 and R are set to 2 nF and 100 kΩ, respectively.

To analyze the energy harvesting performance of RS and SECE circuits, the voltage and power outputs of both circuits are compared in Fig. 22. Notably, the RMS value of power is used for this analysis. Figure 22(*a*) shows that as resistance increases, the voltage growth of the RS circuit becomes less pronounced, showing a trend toward saturation. Compared to the RS circuit, the voltage output of the SECE circuit can rise to a much higher level, implying superior efficiency, even under large load conditions. As shown in Fig. 22(*b*), the SECE circuit delivers a higher and more stable RMS power output than the RS circuit across the entire resistance range. The RMS power of the RS circuit reaches the peak at a resistance of 100 kΩ and then decreases as the resistance further increases. Due to its load-independent nature, the SECE circuit is particularly well-suited for practical applications with time-varying loads.

5 Experimental Validation

To validate the enhanced performance and load independence characteristics of the SP-SECE circuit, we experimentally evaluated a prototyped PDSB shunted to an SP-SECE circuit implemented on a printed circuit board (PCB).

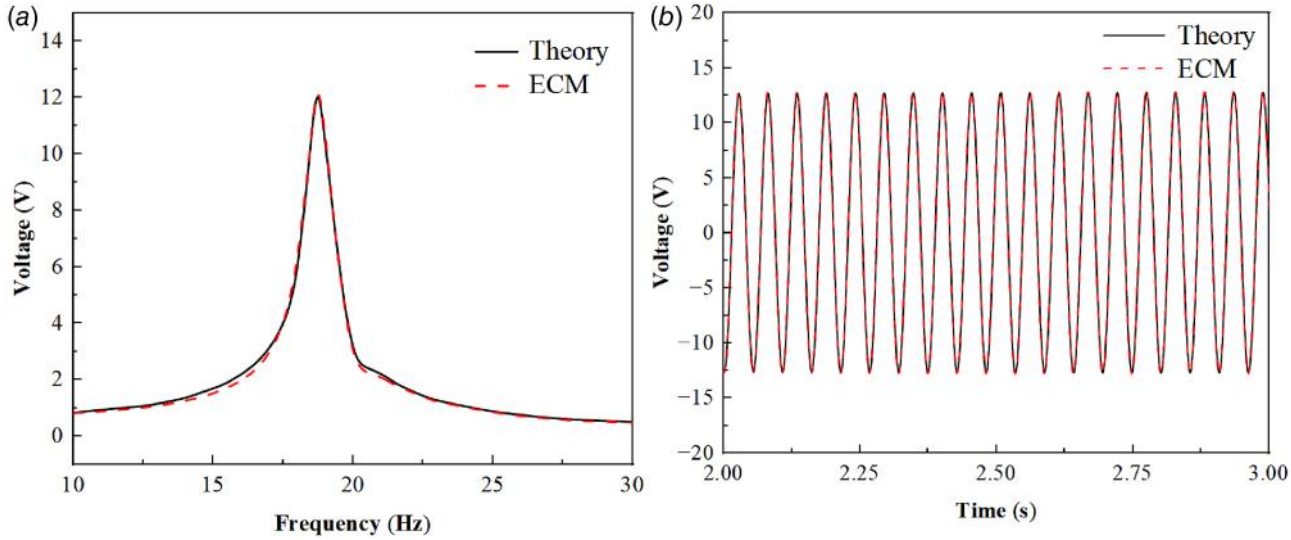

Fig. 18 Comparison of the theoretical model and ECM: (*a*) output voltage; (*b*) time-domain response curve at = 18.73 Hz

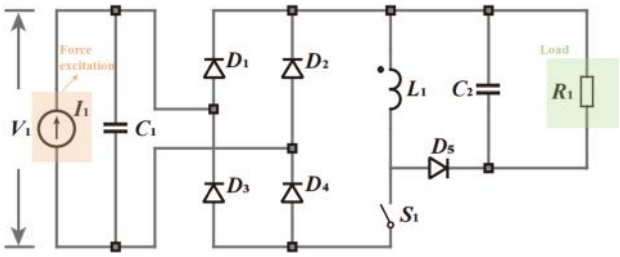

Fig. 19 Schematic of the SECE circuit

Figure 23 presents the experimental platform used to evaluate the SP-SECE circuit. The prototyped PDSB is mounted on a shaker (Econ©, EDS, China). Due to the structural complexity and brittleness of the resin, the left end of the PDSB is rigidly fixed to minimize deformation caused by gravity or bolt preload. The material properties and structural specifications are listed in Table 7. A piezoelectric patch (PZT-5H) with an internal capacitance of 147.2 nF is bonded at the beam root. The system exhibits a resonant frequency of 37.5 Hz. Excitation is applied via a power amplifier (Econ©, VSA-H102A) driving the shaker, while a vibration controller (Econ©, VT-9002) regulates the applied acceleration based on feedback from an accelerometer (Econ©, EV4100). The working waveforms of the SP-SECE circuit are captured and analyzed using an oscilloscope (KEYSIGHT©, DSOX4104A).

Figure 24 shows the open-circuit voltage time responses of the SECE and RS circuits under 37.5 Hz and 1 g excitation. The experimental waveforms in Fig. 24(*a*) illustrate that the SP-SECE circuit successfully performs synchronous switching actions near the voltage peaks. A slight phase lag between the peak voltage and the switching instants is attributed to parasitic effects in the SP-SECE circuit. In addition, the voltage amplitude is amplified by the SP-SECE circuit compared with the open-circuit case. This behavior reflects the weak electromechanical coupling of the prefabricated PDSB, which benefits energy harvesting performance, as the advantage of the SECE technique diminishes in systems with stronger coupling.

Figure 25 presents the experimentally measured output voltage and power of the SP-SECE circuit under 1 g, 37.5 Hz excitation. As shown in Fig. 25(*a*), the output voltage increases with R_L, while the output power, as illustrated in Fig. 25(*b*), remains nearly constant around 35 μW over a R_L range of 0.02–3.0 MΩ. These results validate the enhanced performance and load-independent characteristic of the SECE technique, providing

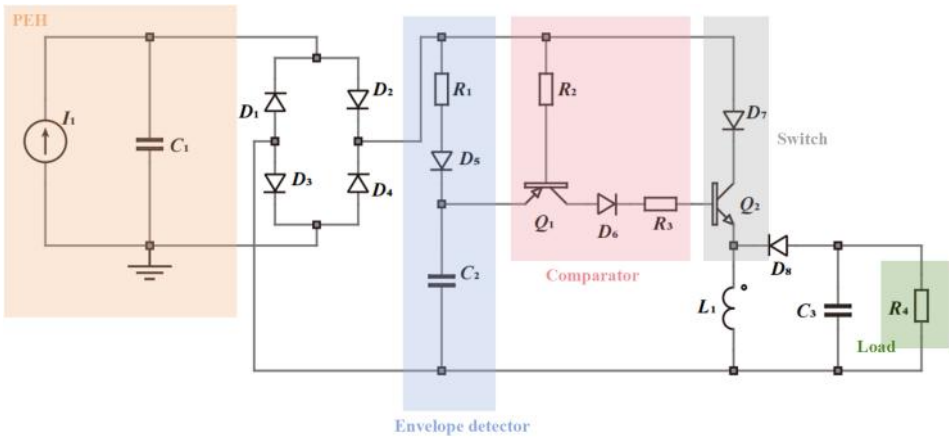

Fig. 20 Schematic of the SP-SECE interface circuit

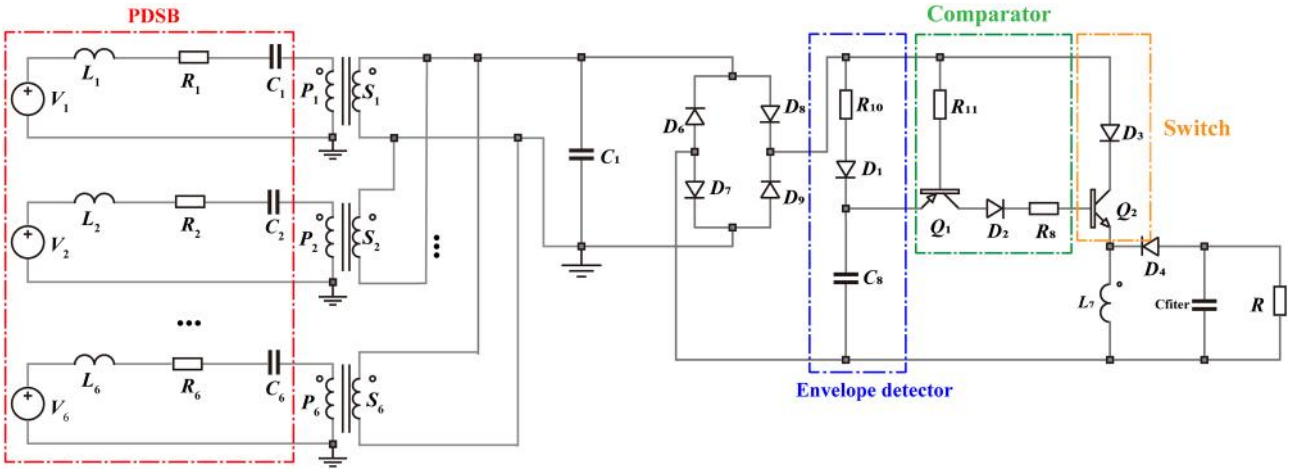

Fig. 21 Circuit representation of the PDSB shunted to an SECE circuit

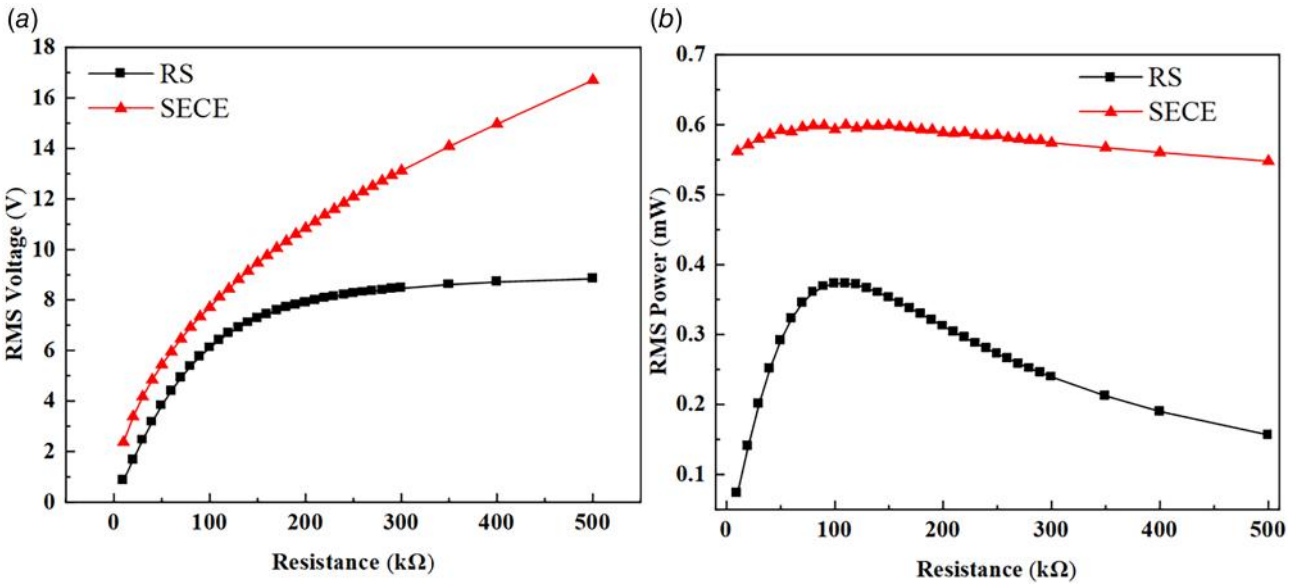

Fig. 22 Comparison of the SECE and RS circuits: (*a*) RMS voltage; (*b*) RMS power

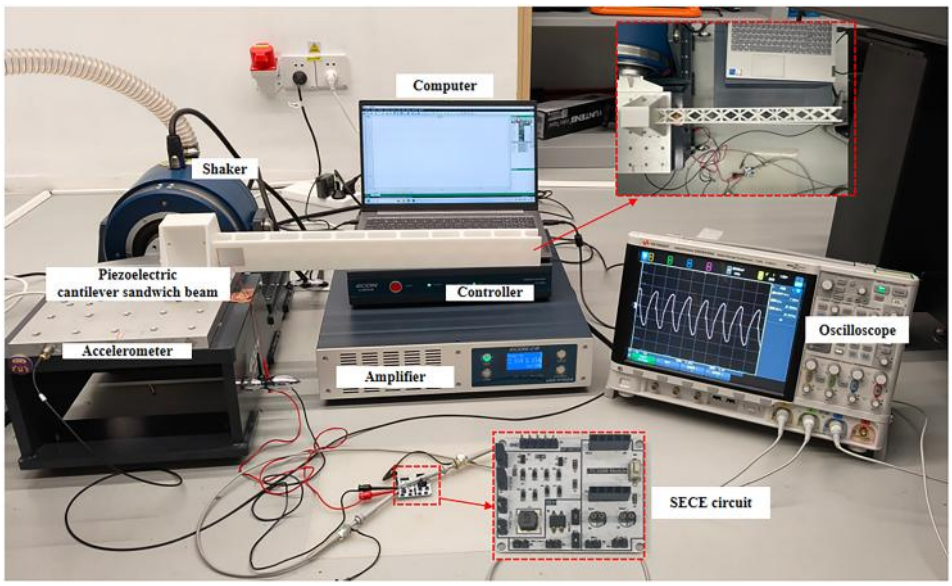

Fig. 23 Experimental setup

Table 7 Materials and structural parameters of the 3D-printed PDSB prototype

L (m)	b (m)	r_1 (m)	r_2 (m)	ρ_f (g/cm^3)	L_p (m)	b_c (m)	h_t (m)	h_c (m)	h_d (m)
0.5	0.05	0.3	0.4	1.3	0.04	0.03	0.01	0.03	0.0002

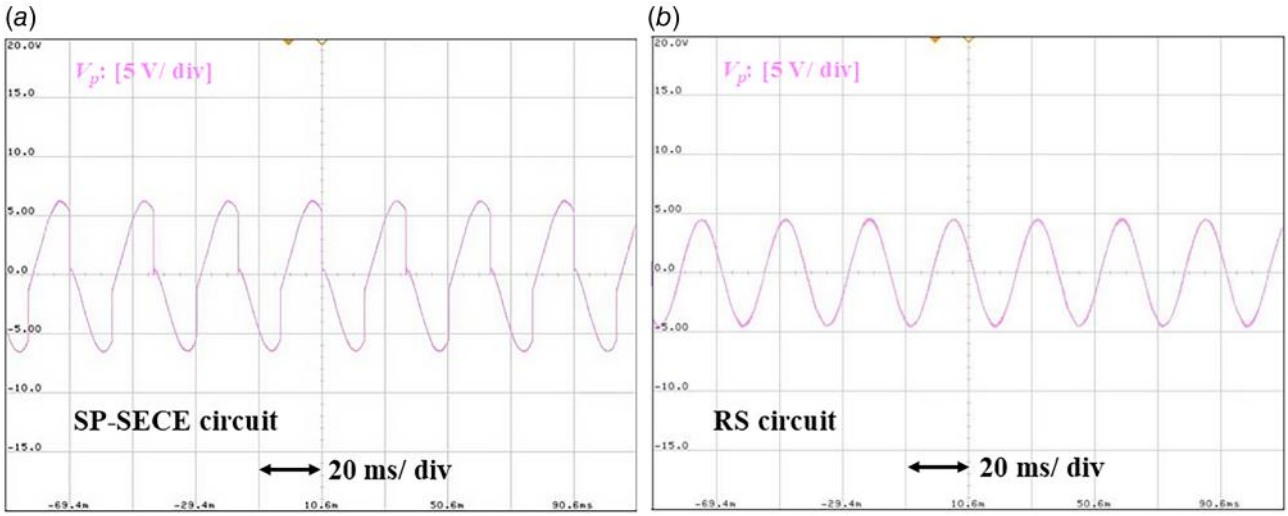

Fig. 24 Experimental waveforms: (*a*) Working voltage waveform of the SP-SECE circuit; (*b*) open-circuit voltage waveform of the RS circuit.

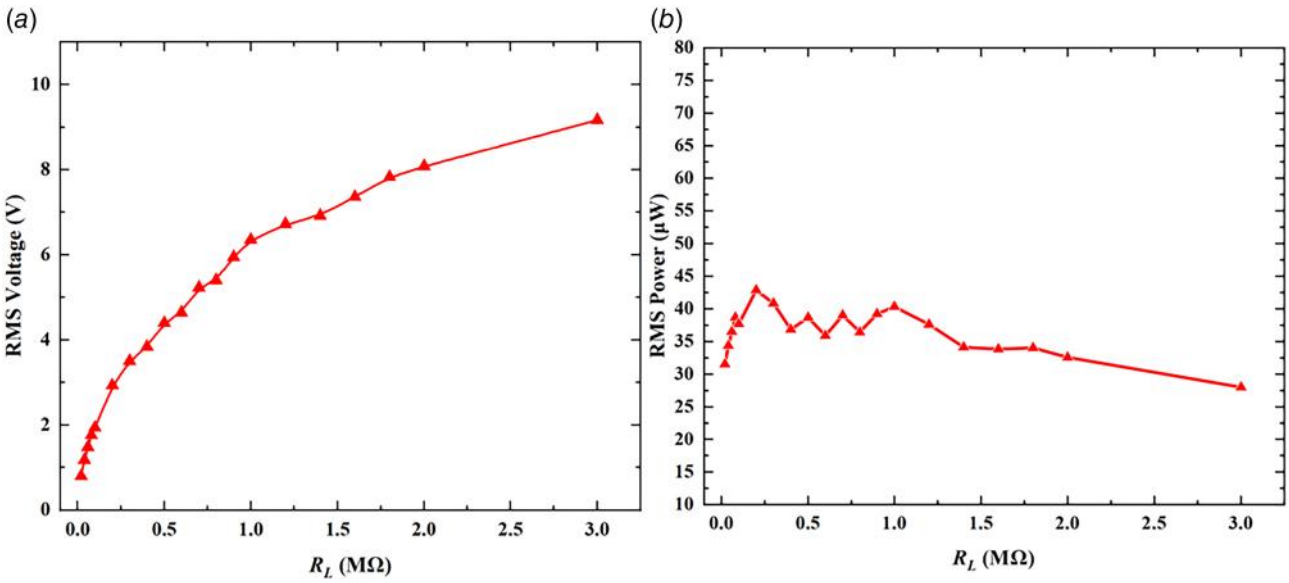

Fig. 25 Experimental results of a PDSB connected to the SP-SECE circuit: (*a*) output voltage versus the load resistance; (*b*) output power versus the load resistance

valuable insights for designing PDSBs with improved energy harvesting capability using advanced nonlinear interface circuits.

6 Conclusion

This paper has presented an innovative piezoelectric energy harvester utilizing a diatomic sandwich beam (referred to as PDSB in this study), with its superior performance demonstrated through theoretical modeling, finite element (FE) analysis, and experimental validation. The governing equations were derived using the homogenization method combined with Hamilton's principle, and a mathematical model of the PDSB incorporating electromechanical coupling effect was formulated using the Lagrange equation. The theoretical results have been compared with those of FE simulations. A good agreement was observed in the estimation of natural frequencies, displacement response, and voltage output, verifying the accuracy of the developed theoretical model. Due to the hourglass-shaped core structure, the PDSB

proposed in this study has shown superior performance in vibration energy harvesting. Compared with a traditional piezoelectric energy harvester using a uniform beam, the PDSB produces a 2.67 times higher voltage output and a 7.14 times higher power output. Moreover, it exhibits a broader operation bandwidth as well. A study has further investigated the influences of the geometric and material parameters on the energy harvesting performance of the PDSB, thereby providing a theoretical foundation for the design optimization. The results have indicated that the power and voltage outputs of the PDSB can be enhanced by using high-density materials for the core layer. A parametric study has offered insights into the design flexibility of the PDSB.

In addition, this study has established the first-ever equivalent circuit model (ECM) for this PDSB, which represents a sandwich beam-based piezoelectric energy harvester. Such an ECM method can also be universally applied to analyze any other sandwich-type piezoelectric energy harvesters. The ECM facilitates the integration of any shunt circuit for a comprehensive system-level analysis. On that basis, we employed a synchronized charge extraction (SECE) circuit to further improve energy harvesting efficiency from the circuit design perspective. Experimental verification further confirmed the reliability of the theory and simulation: using a 3D-printed PDSB prototype, under 1 g excitation, the SECE circuit achieved a maximum power output of 42.85 mW and maintained stable power output within the load range of 0.02 MΩ–3.0 MΩ, demonstrating performance superior to that of traditional resistive shunt circuits. Our study has demonstrated that using the SECE circuit significantly enhances both power output and stability compared to a traditional resistive shunt (RS) circuit. The load-independent nature of the SECE circuit makes it particularly suitable for powering real electronic devices featuring time-varying loads in practical applications.

In summary, this study has proposed an innovative piezoelectric energy harvester based on sandwich structures, established modeling approaches, and conducted experimental tests for validation. The approaches and findings presented in this work have opened the path for the development of sandwich beam-type energy harvesters toward real applications.

Funding Data

- The National Natural Science Foundation of China (Grant Nos. 12472004 and 52305135).
- Guangzhou Municipal Science and Technology Bureau (Grant Nos. SL2023A03J00869 and SL2023A04J01741).
- Guangdong Provincial Key Lab of Integrated Communication, Sensing and Computation for Ubiquitous Internet of Things (Grant No. 2023B1212010007).
- Guangzhou Municipal Key Laboratory on Future Networked Systems (Grant No. 024A03J0623).
- Guangdong Provincial Project (Grant No. 2023QN10L545).
- Nansha District Science and Technology Plan Project (Grant No. 2024ZD008).

Conflict of Interest

There are no conflicts of interest.

Data Availability Statement

The datasets generated and supporting the findings of this article are obtainable from the corresponding author upon reasonable request.

Appendix A

$$[\,J_{p1} \quad J_{p2}\,] = b\int_{h_c/2+h_f}^{h_c/2+h_f+h_d} \frac{e_{31}}{h_d}[\,1 \quad z-\frac{h_c}{2}\,]dz = [\,be_{31} \quad \frac{be_{31}(2h_f+h_d)}{2}\,] \tag{A1}$$

The stiffness expressions are as follows:

$$\begin{aligned} k_{jm}^{aa} = {} & \frac{1}{2}G_1h_cb\left(\int_0^{L_1}\frac{\partial\varphi(x)}{\partial x}\frac{\partial^T\varphi(x)}{\partial x}dx+\int_{L_2}^{L_3}\frac{\partial\varphi(x)}{\partial x}\frac{\partial^T\varphi(x)}{\partial x}dx+\ldots+\int_{L_{18}}^{L_{19}}\frac{\partial\varphi(x)}{\partial x}\frac{\partial^T\varphi(x)}{\partial x}dx\right) \\ & +\frac{1}{2}G_2h_cb\left(\int_{L_1}^{L_2}\frac{\partial\varphi(x)}{\partial x}\frac{\partial^T\varphi(x)}{\partial x}dx+\int_{L_3}^{L_4}\frac{\partial\varphi(x)}{\partial x}\frac{\partial^T\varphi(x)}{\partial x}dx+\ldots+\int_{L_{19}}^{L_{20}}\frac{\partial\varphi(x)}{\partial x}\frac{\partial^T\varphi(x)}{\partial x}dx\right) \\ & +\frac{1}{3}Ebh_f^3\int_0^L\frac{\partial^2\varphi(x)}{\partial x^2}\left(\frac{\partial^2\varphi(x)}{\partial x^2}\right)^T dx \end{aligned} \tag{A2}$$

$$\begin{aligned} k_{jm}^{ac} = {} & -G_1h_cb\left(\int_0^{L_1}\frac{\partial\varphi(x)}{\partial x}\eta^T(x)dx+\int_{L_2}^{L_3}\frac{\partial\varphi(x)}{\partial x}\eta^T(x)dx+\ldots+\int_{L_{18}}^{L_{19}}\frac{\partial\varphi(x)}{\partial x}\eta^T(x)dx\right) \\ & -G_2h_cb\left(\int_{L_1}^{L_2}\frac{\partial\varphi(x)}{\partial x}\eta^T(x)dx+\int_{L_3}^{L_4}\frac{\partial\varphi(x)}{\partial x}\eta^T(x)dx+\ldots+\int_{L_{19}}^{L_{20}}\frac{\partial\varphi(x)}{\partial x}\eta^T(x)dx\right) \\ & +\frac{1}{2}Ebh_ch_f^2\int_0^L\frac{\partial^2\varphi(x)}{\partial x^2}\frac{\partial^T\eta(x)}{\partial x}dx \end{aligned} \tag{A3}$$

$$\begin{aligned} k_{jm}^{cc} = {} & G_1h_cb\left(\int_0^{L_1}\eta(x)\eta^T(x)dx+\int_{L_2}^{L_3}\eta(x)\eta^T(x)dx+\ldots+\int_{L_{18}}^{L_{19}}\eta(x)\eta^T(x)dx\right) \\ & +G_2h_cb\left(\int_{L_1}^{L_2}\eta(x)\eta^T(x)dx+\int_{L_3}^{L_4}\eta(x)\eta^T(x)dx+\ldots+\int_{L_{19}}^{L_{20}}\eta(x)\eta^T(x)dx\right)+\frac{1}{2}Ebh_c^2h_f\int_0^L\frac{\partial\eta(x)}{\partial x}\frac{\partial^T\eta(x)}{\partial x}dx \end{aligned} \tag{A4}$$

$$\mathbf{K} = \begin{bmatrix} k_{jm}^{aa} & k_{jm}^{ac} \\ k_{jm}^{Tac} & k_{jm}^{cc} \end{bmatrix} \tag{A5}$$

The mass expressions are as follows:

$$\begin{aligned} m_{jm}^{aa} = &\left(\frac{1}{2}\bar{\rho}_1 b h_c + h_f b \rho_f\right)\left(\int_0^{L_1} \varphi(x)\varphi^T(x)dx + \int_{L_2}^{L_3} \varphi(x)\varphi^T(x)dx + \ldots + \int_{L_{18}}^{L_{19}} \varphi(x)\varphi^T(x)dx\right) \\ &\left(\frac{1}{2}\bar{\rho}_2 b h_c + h_f b \rho_f\right)\left(\int_{L_1}^{L_2} \varphi(x)\varphi^T(x)dx + \int_{L_3}^{L_4} \varphi(x)\varphi^T(x)dx + \ldots + \int_{L_{19}}^{L_{20}} \varphi(x)\varphi^T(x)dx\right) + \frac{2}{3} b \rho_f h_f^3 \int_0^L \frac{\partial \varphi(x)}{\partial x}\frac{\partial^T \varphi(x)}{\partial x}dx \end{aligned} \tag{A6}$$

$$m_{jm}^{ac} = \frac{1}{2} b \rho_f h_c h_f^2 \int_0^L \frac{\partial \varphi(x)}{\partial x}\eta^T(x)dx \tag{A7}$$

$$\begin{aligned} m_{jm}^{cc} = &\left(\frac{1}{2} b \rho_f h_c^2 h_f + \frac{1}{12} b \bar{\rho}_1 h_c^3\right)\left(\int_0^{L_1} \eta(x)\eta^T(x)dx + \int_{L_2}^{L_3} \eta(x)\eta^T(x)dx + \ldots + \int_{L_{18}}^{L_{19}} \eta(x)\eta^T(x)dx\right) \\ &+ \left(\frac{1}{2} b \rho_f h_c^2 h_f + \frac{1}{12} b \bar{\rho}_2 h_c^3\right)\left(\int_{L_1}^{L_2} \eta(x)\eta^T(x)dx + \int_{L_3}^{L_4} \eta(x)\eta^T(x)dx + \ldots + \int_{L_{19}}^{L_{20}} \eta(x)\eta^T(x)dx\right) \end{aligned} \tag{A8}$$

$$\mathbf{M} = \begin{bmatrix} m_{jm}^{aa} & m_{jm}^{ac} \\ m_{jm}^{Tac} & m_{jm}^{cc} \end{bmatrix} \tag{A9}$$

The electromechanical coupling coefficients are as follows:

$$\zeta_j^a = -e_{31} b \left(\frac{h_d}{2} + h_f\right)\int_0^{L_p} \frac{\partial^2 \varphi(x)}{\partial x^2}dx \tag{A10}$$

$$\zeta_j^c = -e_{31} b h_c \int_0^{L_p} \frac{\partial \eta(x)}{\partial x}dx \tag{A11}$$

$$\begin{aligned} \zeta_j^c = -e_{31} b h_c \int_0^{L_p} \frac{\partial \eta(x)}{\partial x}dx p_j = &b\bar{\rho}_1 h_c\left(\int_0^{L_1} \varphi(x)dx + \int_{L_2}^{L_3} \varphi(x)dx + \ldots + \int_{L_{18}}^{L_{19}} \varphi(x)dx\right) + \\ &b\bar{\rho}_2 h_c\left(\int_{L_1}^{L_2} \varphi(x)dx + \int_{L_3}^{L_4} \varphi(x)dx + \ldots + \int_{L_{19}}^{L_{20}} \varphi(x)dx\right) + b\rho_p h_d \int_0^{L_p} \varphi(x)dx + 2b\rho_f h_f \int_0^L \varphi(x)dx \end{aligned} \tag{A12}$$

Appendix B

Mechanical impedance matrix is expressed as

$$\boldsymbol{\varsigma}^a = -\omega^2 \mathbf{m}^{aa} + j\omega \mathbf{s}^{aa} + \mathbf{k}^{aa} + j\omega\left(j\omega C_p + \frac{1}{R}\right)^{-1} \boldsymbol{\zeta}^a (\boldsymbol{\zeta}^a)^T \tag{B1}$$

$$\boldsymbol{\varsigma}^{ac} = -\omega^2 \mathbf{m}^{ac} + j\omega \mathbf{s}^{ac} + \mathbf{k}^{ac} + j\omega\left(j\omega C_p + \frac{1}{R}\right)^{-1} \boldsymbol{\zeta}^a (\boldsymbol{\zeta}^c)^T \tag{B2}$$

$$\boldsymbol{\varsigma}^a = -\omega^2 \mathbf{m}^{cc} + j\omega \mathbf{s}^{cc} + \mathbf{k}^{cc} + j\omega\left(j\omega C_p + \frac{1}{R}\right)^{-1} \boldsymbol{\zeta}^c (\boldsymbol{\zeta}^c)^T \tag{B3}$$

For short-circuit ($R \to 0$) condition, one can get

$$\boldsymbol{\varsigma}^a = -\omega^2 \mathbf{m}^{aa} + j\omega \mathbf{s}^{aa} + \mathbf{k}^{aa} \tag{B4}$$

$$\boldsymbol{\varsigma}^{ac} = -\omega^2 \mathbf{m}^{ac} + j\omega \mathbf{s}^{ac} + \mathbf{k}^{ac} \tag{B5}$$

$$\boldsymbol{\varsigma}^a = -\omega^2 \mathbf{m}^{cc} + j\omega \mathbf{s}^{cc} + \mathbf{k}^{cc} \tag{B6}$$

For open-circuit ($R \to \infty$), one can get

$$\boldsymbol{\varsigma}^a = -\omega^2 \mathbf{m}^{aa} + j\omega \mathbf{s}^{aa} + \mathbf{k}^{aa} + \frac{1}{C_p} \boldsymbol{\zeta}^a (\boldsymbol{\zeta}^a)^T \tag{B7}$$

$$\boldsymbol{\varsigma}^{ac} = -\omega^2 \mathbf{m}^{ac} + j\omega \mathbf{s}^{ac} + \mathbf{k}^{ac} + \frac{1}{C_p}\boldsymbol{\zeta}^{a}(\boldsymbol{\zeta}^{c})^{T} \tag{B8}$$

$$\boldsymbol{\varsigma}^{a} = -\omega^2 \mathbf{m}^{cc} + j\omega \mathbf{s}^{cc} + \mathbf{k}^{cc} + \frac{1}{C_p}\boldsymbol{\zeta}^{c}(\boldsymbol{\zeta}^{c})^{T} \tag{B9}$$

Appendix C

The stiffness expressions are as follows:

$$\begin{aligned} k_{11} = {} & \frac{1}{2}G_1 h_c b\left(\int_0^{L_1}\frac{\partial\varphi(x)}{\partial x}\frac{\partial^T\varphi(x)}{\partial x}dx + \int_{L_2}^{L_3}\frac{\partial\varphi(x)}{\partial x}\frac{\partial^T\varphi(x)}{\partial x}dx + \ldots + \int_{L_{18}}^{L_{19}}\frac{\partial\varphi(x)}{\partial x}\frac{\partial^T\varphi(x)}{\partial x}dx\right) \\ & + \frac{1}{2}G_2 h_c b\left(\int_{L_1}^{L_2}\frac{\partial\varphi(x)}{\partial x}\frac{\partial^T\varphi(x)}{\partial x}dx + \int_{L_3}^{L_4}\frac{\partial\varphi(x)}{\partial x}\frac{\partial^T\varphi(x)}{\partial x}dx + \ldots + \int_{L_{19}}^{L_{20}}\frac{\partial\varphi(x)}{\partial x}\frac{\partial^T\varphi(x)}{\partial x}dx\right) \\ & + \frac{1}{3}Ebh_f^3\int_0^{L}\frac{\partial^2\varphi(x)}{\partial x^2}\left(\frac{\partial^2\varphi(x)}{\partial x^2}\right)^{T}dx + E_p b\left(h_f^2 h_d + h_f h_d^2 + \frac{h_d^3}{3}\right)\int_0^{L_p}\frac{\partial^2\varphi(x)}{\partial x^2}\left(\frac{\partial^2\varphi(x)}{\partial x^2}\right)^{T}dx \end{aligned} \tag{C1}$$

$$\begin{aligned} k_{12} = {} & -G_1 h_c b\left(\int_0^{L_1}\frac{\partial\varphi(x)}{\partial x}\eta^T(x)dx + \int_{L_2}^{L_3}\frac{\partial\varphi(x)}{\partial x}\eta^T(x)dx + \ldots + \int_{L_{18}}^{L_{19}}\frac{\partial\varphi(x)}{\partial x}\eta^T(x)dx\right) \\ & - G_2 h_c b\left(\int_{L_1}^{L_2}\frac{\partial\varphi(x)}{\partial x}\eta^T(x)dx + \int_{L_3}^{L_4}\frac{\partial\varphi(x)}{\partial x}\eta^T(x)dx + \ldots + \int_{L_{19}}^{L_{20}}\frac{\partial\varphi(x)}{\partial x}\eta^T(x)dx\right) \\ & + \frac{1}{2}Ebh_c h_f^2\int_0^{L}\frac{\partial^2\varphi(x)}{\partial x^2}\frac{\partial^T\eta(x)}{\partial x}dx + \left(\frac{1}{2}E_p b(\frac{1}{2}h_c^2 h_d + \frac{1}{2}h_c h_d^2 + h_f h_c h_d) - \frac{1}{4}E_p b h_d h_c^2\right)\int_0^{L_p}\frac{\partial^2\varphi(x)}{\partial x^2}\eta^T(x)dx \end{aligned} \tag{C2}$$

$$\begin{aligned} k_{22} = {} & G_1 h_c b\left(\int_0^{L_1}\eta(x)\eta^T(x)dx + \int_{L_2}^{L_3}\eta(x)\eta^T(x)dx + \ldots + \int_{L_{18}}^{L_{19}}\eta(x)\eta^T(x)dx\right) \\ & + G_2 h_c b\left(\int_{L_1}^{L_2}\eta(x)\eta^T(x)dx + \int_{L_3}^{L_4}\eta(x)\eta^T(x)dx + \ldots + \int_{L_{19}}^{L_{20}}\eta(x)\eta^T(x)dx\right) \\ & + \frac{1}{2}Ebh_c^2 h_f\int_0^{L}\frac{\partial\eta(x)}{\partial x}\frac{\partial^T\eta(x)}{\partial x}dx + \frac{1}{4}E_p b h_c^2 h_d\int_0^{L_p}\frac{\partial\eta(x)}{\partial x}\frac{\partial^T\eta(x)}{\partial x}dx \end{aligned} \tag{C3}$$

$$\mathrm{K}_1 = \begin{bmatrix} k_{11} & k_{12} \\ k_{12}^T & k_{22} \end{bmatrix} \tag{C4}$$

The mass expressions are as follows:

$$\begin{aligned} m_{11} = {} & \left(\frac{1}{2}\bar{\rho}_1 b h_c + h_f b\rho_f\right)\left(\int_0^{L_1}\varphi(x)\varphi^T(x)dx + \int_{L_2}^{L_3}\varphi(x)\varphi^T(x)dx + \ldots + \int_{L_{18}}^{L_{19}}\varphi(x)\varphi^T(x)dx\right. \\ & \times \left(\frac{1}{2}\bar{\rho}_2 b h_c + h_f b\rho_f\right)\left(\int_{L_1}^{L_2}\varphi(x)\varphi^T(x)dx + \int_{L_3}^{L_4}\varphi(x)\varphi^T(x)dx + \ldots + \int_{L_{19}}^{L_{20}}\varphi(x)\varphi^T(x)dx\right) + \frac{2}{3}b\rho_f h_f^3\int_0^{L}\frac{\partial\varphi(x)}{\partial x}\frac{\partial^T\varphi(x)}{\partial x}dx \\ & + b\rho_p h_d\int_0^{L_p}\varphi(x)\varphi^T(x)dx \end{aligned} \tag{C5}$$

$$m_{12} = \frac{1}{2}b\rho_f h_c h_f^2\int_0^{L}\frac{\partial\varphi(x)}{\partial x}\eta^T(x)dx + \frac{1}{2}b\rho_p(h_c h_d^2 + h_c h_d h_f)\int_0^{L}\frac{\partial\varphi(x)}{\partial x}\eta^T(x)dx \tag{C6}$$

$$\begin{aligned} m_{22} = {} & \left(\frac{1}{2}b\rho_f h_c^2 h_f + \frac{1}{12}b\bar{\rho}_1 h_c^3\right)\left(\int_0^{L_1}\eta(x)\eta^T(x)dx + \int_{L_2}^{L_3}\eta(x)\eta^T(x)dx + \cdots + \int_{L_{18}}^{L_{19}}\eta(x)\eta^T(x)dx\right) \\ & + \left(\frac{1}{2}b\rho_f h_c^2 h_f + \frac{1}{12}b\bar{\rho}_2 h_c^3\right)\left(\int_{L_1}^{L_2}\eta(x)\eta^T(x)dx + \int_{L_3}^{L_4}\eta(x)\eta^T(x)dx + \cdots + \int_{L_{19}}^{L_{20}}\eta(x)\eta^T(x)dx\right) + \frac{1}{4}b\rho_p h_d h_c^2\int_0^{L_p}\eta(x)\eta^T(x)dx \end{aligned} \tag{C7}$$

$$M_1 = \begin{bmatrix} m_{11} & m_{12} \\ m_{12}^T & m_{22} \end{bmatrix} \tag{C8}$$

References

[1] Zeng, S., Tanveer, A., Fu, X., Gu, Y., and Irfan, M., 2022, "Modeling the Influence of Critical Factors on the Adoption of Green Energy Technologies," Renew. Sustainable Energy Rev., **168**, p. 112817.

[2] Liu, H., Fu, H., Sun, L., Lee, C., and Yeatman, E. M., 2020, "Hybrid Energy Harvesting Technology: From Materials, Structural Design, System Integration to Applications," Renew. Sustainable Energy Rev., p. 110473.

[3] Sun, R., Ma, H., Zhou, S., Li, Z., and Cheng, L., 2024, "A Direction-Adaptive Ultra-Low Frequency Energy Harvester With an Aligning Turntable," Energy, **311**, p. 133273.

[4] Sun, R., Zhou, S., Li, Z., and Cheng, L., 2024, "Dual Electromagnetic Mechanisms With Internal Resonance for Ultra-Low Frequency Vibration Energy Harvesting," Appl. Energy, **369**, p. 123528.

[5] Yang, T., Zhou, S., Fang, S., Qin, W., and Inman, D. J., 2021, "Nonlinear Vibration Energy Harvesting and Vibration Suppression Technologies: Designs, Analysis, and Applications," Appl. Phys. Rev., **8**(3), p. 031317.

[6] Wei, C., and Jing, X., 2017, "A Comprehensive Review on Vibration Energy Harvesting: Modelling and Realization," Renew. Sustainable Energy Rev., **74**, pp. 1–18.

[7] Shi, Y., Song, Q. H., Toftul, I., Zhu, T., Yu, Y., Zhu, W. M., Tsai, D. P., Kivshar, Y. A., and Liu, A. Q., 2022, "Optical Manipulation with Metamaterial Structures," Appl. Phys. Rev., **9**(3).

[8] Paranjape, M. V., Graham, S. A., Patnam, H., Manchi, P., and Yu, J. S., 2021, "3D Printed Bidirectional Rotatory Hybrid Nanogenerator for Mechanical Energy Harvesting," Nano Energy, **88**, p. 106250.

[9] An, X., Yuan, X., Sun, G., He, W., Lai, C., Hou, X., and Fan, H., 2024, "Sandwich Plate-Type Metastructures With Periodic Graded Resonators for Low-Frequency and Broadband Vibration Attenuation," Ocean Eng., **298**, p. 117229.

[10] Chai, Y., Li, F., Song, Z., and Zhang, C., 2020, "Influence of the Boundary Relaxation on the Flutter and Thermal Buckling of Composite Laminated Panels," Aerosp. Sci. Technol., **104**, p. 106000.

[11] Gong, C., Ritchie, R. O., Wei, X., Liu, Q., and Xiong, J., 2025, "Mechanical Properties of Modular Assembled Composite Lattice Architecture," J. Mech. Phys. Solids, **195**, p. 105967.

[12] Li, H.-Z., Yang, J.-S., Liu, Q., Li, S., Liu, X., Yang, F., and Wu, L.-Z., 2024, "A Novel Sandwich Structure for Integrated Sound Insulation and Absorption," Int. J. Mech. Sci., **279**, p. 109526.

[13] Wei, X., Jiao, Y., Wang, Y., Yan, C., Han, J., and Xiong, J., 2024, "Surface Matching Design of Carbon Fiber Composite Honeycomb," J. Mech. Phys. Solids, **193**, p. 105890.

[14] Wang, W.-J., Yang, H., Zhang, W.-M., Shang, N., and Ma, L., 2025, "Experimental Study on the Impact Resistance of Fill-Enhanced Mechanical Metamaterials," Int. J. Mech. Sci., **285**, p. 109799.

[15] Zang, J., Chen, B., Song, X., Zhang, Z., Zhang, Y.-W., and Chen, L.-Q., 2025, "Vibration of Composite Laminated Airfoil-Beam-Structures of Electric Aircraft in Hygrothermal Environment: Theory Formulation and Experimental Investigation," Compos. Struct., **354**, p. 118781.

[16] Jiang, G., and Li, F., 2018, "Aerothermoelastic Analysis of Composite Laminated Trapezoidal Panels in Supersonic Airflow," Compos. Struct., **200**, pp. 313–327.

[17] Li, F., and Lyu, X., 2014, "Active Vibration Control of Lattice Sandwich Beams Using the Piezoelectric Actuator/Sensor Pairs," Compos. Part B: Eng., **67**, pp. 571–578.

[18] Zhao, Z., Wen, S., and Li, F., 2018, "Vibration Analysis of Multi-Span Lattice Sandwich Beams Using the Assumed Mode Method," Compos. Struct., **185**, pp. 716–727.

[19] Li, M., Du, S., Li, F., and Jing, X., 2020, "Vibration Characteristics of Novel Multilayer Sandwich Beams: Modelling, Analysis and Experimental Validations," Mech. Syst. Signal Process., **142**, p. 106799.

[20] Zhang, Y., Fan, X., Li, J., Li, F., Yu, G., Zhang, R., and Yuan, K., 2021, "Low-Frequency Vibration Insulation Performance of the Pyramidal Lattice Sandwich Metamaterial Beam," Compos. Struct., **278**, p. 114719.

[21] Li, H., Hu, Y., Huang, H., Chen, J., Zhao, M., and Li, B., 2021, "Broadband Low-Frequency Vibration Attenuation in 3D Printed Composite Meta-Lattice Sandwich Structures," Compos. Part B: Eng., **215**, p. 108772.

[22] Guo, J., Li, Y., Xiao, Y., Fan, Y., Yu, D., and Wen, J., 2022, "Multiscale Modeling and Design of Lattice Truss Core Sandwich Metastructures for Broadband Low-Frequency Vibration Reduction," Compos. Struct., **289**, p. 115463.

[23] Yu, D., Hu, G., Guo, Z., Hong, J., and Yang, Y., 2023, "Topological Interface State Formation in an Hourglass Lattice Sandwich Meta-Structure," Int. J. Mech. Sci., **246**, p. 108170.

[24] Guo, Z., Wen, J., Yu, D., Hu, G., and Yang, Y., 2023, "Widening the Band Gaps of Hourglass Lattice Truss Core Sandwich Structures for Broadband Vibration Suppression," ASME J. Vib. Acoust., **145**(6), p. 061002.

[25] Lin, Q., Zhou, J., Wang, K., Cai, C., and Wang, Q., 2024, "Enhanced Low-Frequency Band Gap of Nonlinear Quasi-Zero-Stiffness Metamaterial by Lowering Stiffness Coupling," Nonlinear Dyn., pp. 1–20.

[26] Li, Z., Wang, K., Chen, T., Cheng, L., Xu, D., and Zhou, J., 2023, "Temperature Controlled Quasi-Zero-Stiffness Metamaterial Beam for Broad-Range Low-Frequency Band Tuning," Int. J. Mech. Sci., **259**, p. 108593.

[27] Meng, Y., Lu, Z.-Q., Ding, H., and Chen, L.-Q., 2024, "Plate Theory Based Modeling and Analysis of Nonlinear Piezoelectric Composite Circular Plate Energy Harvesters," Nonlinear Dyn., **112**(7), pp. 5129–5149.

[28] Qin, L., Zhang, L., Feng, J., Zhang, F., Han, Q., Qin, Z., and Chu, F., 2024, "A Hybrid Triboelectric-Piezoelectric Smart Squirrel Cage With Self-Sensing and Self-Powering Capabilities," Nano Energy, **124**, p. 109506.

[29] Lu, Z.-Q., Hao, R.-B., Wu, D., Ding, H., and Chen, L.-Q., 2024, "An Investigation of a Self-Powered Low-Frequency Nonlinear Vibration Isolation System," Eng. Struct., **315**, p. 118395.

[30] Lu, Z.-Q., Zhao, L., Fu, H.-L., Yeatman, E., Ding, H., and Chen, L.-Q., 2024, "Ocean Wave Energy Harvesting With High Energy Density and Self-Powered Monitoring System," Nat. Commun., **15**(1), p. 6513.

[31] Wang, Y., Du, H., Yang, H., Xi, Z., Zhao, C., Qian, Z., Chuai, X., et al., 2024, "A Rolling-Mode Triboelectric Nanogenerator With Multi-Tunnel Grating Electrodes and Opposite-Charge-Enhancement for Wave Energy Harvesting," Nat. Commun., **15**(1), p. 6834.

[32] Tran, N., Ghayesh, M. H., and Arjomandi, M., 2018, "Ambient Vibration Energy Harvesters: A Review on Nonlinear Techniques for Performance Enhancement," Int. J. Eng. Sci., **127**, pp. 162–185.

[33] Yildirim, T., Ghayesh, M. H., Li, W., and Alici, G., 2017, "A Review on Performance Enhancement Techniques for Ambient Vibration Energy Harvesters," Renew. Sustainable Energy Rev., **71**, pp. 435–449.

[34] Erturk, A., and Inman, D. J., 2008, "A Distributed Parameter Electromechanical Model for Cantilevered Piezoelectric Energy Harvesters," ASME J. Vib. Acoust., **130**(4), p. 041002.

[35] Erturk, A., and Inman, D. J., 2008, "On Mechanical Modeling of Cantilevered Piezoelectric Vibration Energy Harvesters," J. Intell. Mater. Syst. Struct., **19**(11), pp. 1311–1325.

[36] Xiong, X., and Oyadiji, S. O., 2014, "Modal Electromechanical Optimization of Cantilevered Piezoelectric Vibration Energy Harvesters by Geometric Variation," J. Intell. Mater. Syst. Struct., **25**(10), pp. 1177–1195.

[37] Zhang, Y.-W., Su, C., Ni, Z.-Y., Zang, J., and Chen, L.-Q., 2019, "A Multifunctional Lattice Sandwich Structure With Energy Harvesting and Nonlinear Vibration Control," Compos. Struct., **221**, p. 110875.

[38] Li, Q., Li, S., Zhou, L., Cao, X., Lan, Y., Xu, X., Huang, Y. A., et al., 2023, "Optimal Design Towards High Performance of Sandwich Flexible Piezoelectric Energy Harvesters," ASME J. Appl. Mech., **90**(6), p. 061007.

[39] Aewzipo, N., Olarnrithinun, S., and Aimmanee, S., 2024, "Functionally Varied Negative-Stiffness Metamaterial Core Sandwich Structures With Three-Phase Bending Deformation," Smart Mater. Struct., **33**(5), p. 055018.

[40] Wang, J., Luo, L., Yurchenko, D., and Hu, G., 2024, "Equivalent Circuit Analysis of a Nonlinear Vortex-Induced Vibration Piezoelectric Energy Harvester Using Synchronized Switch Technique," IEEE Trans. Ind. Electron.

[41] Lefeuvre, E., Badel, A., Richard, C., and Guyomar, D., 2005, "Piezoelectric Energy Harvesting Device Optimization by Synchronous Electric Charge Extraction," J. Intell. Mater. Syst. Struct., **16**(10), pp. 865–876.

[42] Yang, Y., and Tang, L., 2009, "Equivalent Circuit Modeling of Piezoelectric Energy Harvesters," J. Intell. Mater. Syst. Struct., **20**(18), pp. 2223–2235.

[43] Fang, S., Miao, G., Chen, K., Xing, J., Zhou, S., Yang, Z., and Liao, W.-H., 2022, "Broadband Energy Harvester for Low-Frequency Rotations Utilizing Centrifugal Softening Piezoelectric Beam Array," Energy, **241**, p. 122833.

[44] Zhang, Z., Xiang, H., Tang, L., and Yang, W., 2022, "A Comprehensive Analysis of Piezoelectric Energy Harvesting From Bridge Vibrations," J. Phys. D: Appl. Phys., **56**(1), p. 014001.

[45] Clementi, G., Costanza, M., Ouhabaz, M., Bartasyte, A., Dulmet, B., and Margueron, S., 2023, "2D + 1 Degree of Freedom Equivalent Circuit Model for LiNbO3/Metal/LiNbO3 Bimorph Bending Cantilever," Sens. Actuators A: Phys., **362**, p. 114606.

[46] Guo, Z., Jiang, S., Shen, Y., Jiang, G., Xiao, B., Xu, Q., and Li, M., 2025, "Nonlinear Dynamic Analysis and Vibration Reduction of two Sandwich Beams Connected by a Joint With Clearance," Mech. Syst. Signal Process., **223**, p. 111828.

[47] Gonçalves, P. J. P., Peplow, A., and Brennan, M. J., 2018, "Exact Expressions for Numerical Evaluation of High Order Modes of Vibration in Uniform Euler-Bernoulli Beams," Appl. Acoust., **141**, pp. 371–373.

[48] Guo, Z., Hu, G., Jiang, J., Yu, L., Li, X., and Liang, J., 2021, "Theoretical and Experimental Study of the Vibration Dynamics of a 3D-Printed Sandwich Beam With an Hourglass Lattice Truss Core," Front. Mech. Eng., **7**, p. 651998.

[49] Zang, J., Ren, H.-M., Song, X.-Y., Zhang, Z., Zhang, Y.-W., and Chen, L.-Q., 2024, "Vibration Control of Interconnected Composite Beams: Dynamical Analysis and Experimental Validations," Mech. Syst. Signal Process., **208**, p. 111008.

[50] Hu, G., Tang, L., Yang, Y., Yu, D., and Zi, Y., 2023, "High-Fidelity Dynamics of Piezoelectric Covered Metamaterial Timoshenko Beams Using the Spectral Element Method," Smart Mater. Struct., **32**(9), p. 095023.

[51] Hu, H., Mei, Z. Y., Li, H., and Wu, D., 2022, "A Comprehensive Investigation on Bending Stiffness of Composite Grid-Stiffened and Functional Foams Sandwich Beam," AIP Adv., **12**(10).

[52] Guo, Z.-K., Yang, X., and Zhang, W., 2020, "Dynamic Analysis, Active and Passive Vibration Control of Double-Layer Hourglass Lattice Truss Structures," J. Sandw. Struct. Mater., **22**(5), pp. 1329–1356.

[53] Li, X., Upadrashta, D., Yu, K., and Yang, Y., 2018, "Sandwich Piezoelectric Energy Harvester: Analytical Modeling and Experimental Validation," Energy Convers. Manage., **176**, pp. 69–85.

[54] Lombardi, G., and Lallart, M., 2021, "Synchronous Electric Charge and Induced Current Extraction (SECICE): A Unified Nonlinear Technique Combining Piezoelectric and Electromagnetic Harvesting," Smart Mater. Struct., **30**(2), p. 025029.

[55] Zhang, Z., Xiang, H., and Tang, L., 2021, "Modeling, Analysis and Comparison of Four Charging Interface Circuits for Piezoelectric Energy Harvesting," Mech. Syst. Signal Process., **152**, p. 107476.

[56] Arroyo, E., and Badel, A., 2011, "Electromagnetic Vibration Energy Harvesting Device Optimization by Synchronous Energy Extraction," Sens. Actuators A: Phys., **171**(2), pp. 266–273.

[57] Jia, S., Zeng, C., Shi, G., Hong, C., Han, J., and Xia, Y., 2023, "A Self-Powered Synchronous Magnetic Flux Extraction Interface for Electromagnetic Energy Harvesting," Microelectron. J., **140**, p. 105943.